IEEE Access
Multidisciplinary | Rapid Review | Open Access Journal

Received 10 January 2024, accepted 22 January 2024, date of publication 31 January 2024, date of current version 7 February 2024.

Digital Object Identifier 10.1109/ACCESS.2024.3360413

RESEARCH ARTICLE

An MB-OFDM Based Wideband THz Communication System With Impairment Aware Precoder and Squint Effect Mitigation

T.D DHEERAJLAL, (Graduate Student Member, IEEE), ANKAM MADHUSREE, (Student Member, IEEE), AND AMIT KUMAR DUTTA, (Member, IEEE)

G. S. Sanyal School of Telecommunications, Indian Institute of Technology Kharagpur, Kharagpur 721302, India

Corresponding author: Amit Kumar Dutta (amitdutta@gssst.iitkgp.ac.in)

This work was supported by the Ministry of Electronics and Information Technology (MeiTY), Government of India, under Grant 13(44)/2020-CC&BT.

ABSTRACT Terahertz (THz) communication is a highly promising solution for addressing the ultra-high data rate requirements of future sixth-generation (6G) wireless systems. However, the unfavorable frequency-dependent channel characteristics of THz communication pose a significant challenge in realizing this promising technology. In this paper, we present a novel solution to this challenge by proposing a wideband THz system featuring a unique THz-specific digital baseband waveform design tailored to the distinctive channel characteristics of the THz spectrum. To address the frequency-dependent challenges posed by the wideband THz channel and the spectral efficiency loss inherent in conventional orthogonal frequency division multiplexing (OFDM) systems due to cyclic prefix overhead, we propose a THz system with beamforming incorporating a multi-band OFDM (MB-OFDM) based waveform design using a filter-bank based channel model that slices the wideband channel into smaller frequency-independent subbands for ultra-wideband THz communication. Furthermore, this work introduces a novel squint model taking into account the printed-circuit-board (PCB) impairments and circuit imperfections, which have not been considered before. We also propose an all-digital mitigation scheme with this model. We propose a channel estimation algorithm using a three-level adaptive method with an auto-regressive (AR) model for exploiting the frequency dependency among the intra and inter-narrow subbands. Apart from these key contributions, we propose a THz environment-aware precoder to mitigate the wideband effect in the THz channel, specifically the subband-specific path loss and environment-related effect, and balance the overall gains across the band. We have also proposed to optimize the number of subbands and zero-padding in MB-OFDM waveform based on the minimum bit error rate (MBER) criterion. Numerical simulations are carried out to evaluate the performance of the proposed schemes demonstrating their feasibility and effectiveness for wideband THz communication with results showing a lower peak-to-average power ratio (PAPR) for the proposed waveform as compared to conventional OFDM.

INDEX TERMS THz communications, THz waveform, MB-OFDM, filter bank, THz channel estimation, AR, LMMSE, digital squint mitigation.

I. INTRODUCTION

The wireless communication in the Terahertz (THz) band is considered to be the most promising solution to support the ultra-high data rate requirements of the next-generation wireless communication networks [1], [2]. The THz band ranges from 100 GHz to 10 THz and provides ultra-wide bandwidth. It promises huge opportunities for research and development, starting from signal processing to circuit design. The THz band will be used for several applications

The associate editor coordinating the review of this manuscript and approving it for publication was Walid Al-Hussaibi.

like pico-cellular indoor communication, future wireless local area networks (WLAN), high-speed wireless links in intelligent vehicular networks, etc.

However, to ensure reliable and efficient wireless communication within the THz spectrum, it is essential to develop a THz-specific waveform that can handle ultra-wide bandwidth and the associated unfavorable wideband THz channel characteristics. These characteristics differ significantly from those found in low-frequency wireless channels. The THz channel is heavily influenced by frequency-dependent molecular absorption loss [3], [4]. Moreover, owing to the distinct properties of the THz band, propagation phenomena such as reflection, scattering, and diffraction also exhibit frequency-dependent behavior [5], [6], [7], particularly as we move higher into the THz frequency ranges. Given these highly frequency-dependent nature, the channel coefficients cannot be treated as constants across the entire bandwidth of interest. Consequently, one of the most critical challenges in the development of future ultra-wideband THz wireless systems is addressing the frequency-dependent nature of the channel impulse response (CIR). However, all the existing THz works fail to address this key issue of the frequency-dependent nature of the channel. However in order to make ultra-wideband wireless communication in the THz band, we need to develop a THz-specific digital waveform that works efficiently and reliably. Channel modelling is the first step toward the design of an ultra-wideband THz-specific waveform.

There are several THz channel models in the literature. In [5] and [6], scattering and roughness analysis have been done for the THz channel. In [8], [9], [10], and [11], propagation characteristics have been modelled for 300 GHz and dispersion model in [12]. An indoor stochastic model for THz channels at 300 GHz is provided in [13]. A propagation model based on radiative transfer theory and molecular absorption is presented in [3]. A multi-ray channel model is developed in [4], as a combination of frequency-independent subchannels in radio frequency (RF). However, the number of such frequency flat subchannels will be very large, which makes channel estimation very difficult. A causal channel model for short-range THz communication based on minimum phase is provided in [14]. A stochastic THz channel model has been proposed in [13]. However, an appropriate digital baseband input-output wideband THz channel model that is suitable for waveform design and development of various baseband signal processing techniques is needed.

Waveform design in the THz band has been attempted in earlier literature. Authors in [15] first proposed a multi-wideband waveform in THz system, which uses narrow pulses. However, the realization of an extremely narrow pulse is very challenging compared to the simplicity in the implementation of the orthogonal frequency division multiplexing (OFDM) system, which has come a long way and has found its place in the fifth-generation (5G) system. Though work in [16] makes a good comparison between single and multi-carrier communication in the THz system, the study does not include the general class of filter bank multi-carrier (FBMC) [17] or more specifically multi-band OFDM (MB-OFDM), which provides a different advantage like spectrum confinement and spectral efficiency improvement. A waveform design for joint sensing and communications in millimeter wave (mmWave) and low THz bands is discussed in recent work [18]. Work in [19] considers a single carrier THz waveform with hierarchical bandwidth modulation, which may not provide spectral efficiency and spectrum confinement by choice.

Motivation for MB-OFDM: There are two key problems that OFDM faces in very large bandwidth systems. The first one is the loss of effective data rate due to huge cyclic prefix (CP) addition, especially when the bandwidth is very large. The second issue is the spectral spillage by OFDM, which causes considerable sideband interference. They can be well mitigated in MB-OFDM with the cost of a front-end filter bank that poses some challenges though. The MB-OFDM system splits the entire large band into smaller subbands. Hence, it needs a smaller CP at each smaller band followed by a front-end filter. This makes the effective CP length very small compared to the single OFDM system at a high bandwidth. The basic structure of MB-OFDM has been proposed in [20] as an alternative to the offset quadrature amplitude modulation (OQAM), that enhances spectral confinement and efficiency with inter-carrier interference presence mainly in the sub-6 GHz. However, this has not been explored considering the wideband THz aspect with beamforming. Similar works are discussed in [21] and [22] with no consideration of the wideband THz aspects. The work in [23] lacks detailed insight for its usage in the context of wideband THz and does not consider beamforming. All these works in [20], [21], [22], and [23] mostly concentrate on the spectral efficiency and out-of-band spectrum leakage, and do not consider the high wideband and THz channel effects. All these works lack the channel estimation part as well.

Literature survey on THz system: There are several works related to the system design in THz with respect to single carrier or single band OFDM system. Work in [24] proposes precoder and detection design for broadband THz system based on the minimum mean square error (MMSE) criterion. This work considers a single carrier system, which may not work well for higher spectral efficiency. Similar recent works can be found in [25], [26], and [27]. The impact of interference and other performance-related analysis in THz systems have been summarized in [28] and [29]. A comprehensive overview of THz communication can be found in [30]. In this work, we consider a digital baseband input-output filter bank channel model for the wideband THz channel based on the parallel finite impulse response (FIR) filters, which is an extension from [4]. The model characterizes both the time and frequency-dependent nature of the THz channel. Using this model, we propose a THz-specific MB-OFDM waveform design deploying beamforming at both the transmitter and receiver.

In this work, we do not focus on the angle of arrival (AoA) and angle of departure (AoD) estimation as in [31], except the overall post-fast Fourier transformation (FFT) channel coefficients (eigenvalues). However, several recent works now exist for the THz channel estimation. A single band OFDM-based multiple input multiple output (MIMO) channel estimation for 5G and beyond communication has been proposed in [32] and [33]. Channel estimation based on deep kernel learning is proposed in [34]. The estimation has also been done for the intelligent reflecting surface (IRS) in the THz channel in [35], [36], and [37]. In [38], a sparse Bayesian learning (SBL) technique for joint channel and beam-split estimation in the THz band by treating the beam-split as an array perturbation is discussed. Another recent work in [39] proposes channel estimation for the wideband MIMO-OFDM THz system using a low-complexity beam squint mitigation scheme with the true-time-delay (TTD) technique. A time-delay unit-based beam squint mitigation for IRS-aided communications in the THz band is given in [40]. The work in [41] proposes an efficient channel estimation algorithm for near-field IRS-assisted wideband THz systems without considering the beam squint effect. Another recent work in [42] also uses a TTD-based technique to mitigate the squint effect. However, the TTD-based systems are costly and highly inefficient as they operate in the RF domain, resulting in significant power consumption and circuit inaccuracies. Additionally, they are unable to effectively address the amplitude distortion caused by impairments on the printed circuit board (PCB) or leverage any statistical properties associated with these impairments.

Contributions: Given this background, the contributions of this work are several and they are described as follows

A. KEY CONTRIBUTIONS

1) *THz-specific MB-OFDM waveform design :* A THz specific waveform design based on MB-OFDM structure has been proposed for very large bandwidth data transmission in THz spectrum based on a digital baseband filter bank wideband THz channel model. The large signal bandwidth is split into several narrow subbands, such that the channel coefficients remain invariant over frequency. In this work, we have also used beamforming at the transmitter and receiver using uniform planar arrays (UPA).
2) *Squint effect model and mitigation:* We have proposed a novel squint modelling and mitigation scheme in the digital domain. It takes into account various hardware impairments present in the PCB, which have not been considered in squint mitigation problems before. The parameters include the wire length, delay mismatch among RF components, phase shifter (PS) mismatch, antenna connectors on board, inaccuracies in digital-to-analog (DAC)/analog-to-digital (ADC) sampling frequency offset (SFO), THz effect on skin depth of the wire and temperature variation. We apply the statistical properties of the impairments and use the linear minimum mean square error (LMMSE) technique for countering these effects in squint mitigation.
3) *Wideband THz channel estimation:* We propose a three-stage channel estimation technique with the exploitation of the intra-subband and inter-subband frequency correlation using non-adaptive and adaptive methods.
    a) In the first stage, the least square (LS) based channel estimation algorithm has been applied to estimate the channel coefficients in the frequency domain corresponding to the pilot positions. In the second stage, an auto-regressive (AR) model is assumed that exploits the intra-subband correlation. We then adopt the LMMSE technique to estimate the channel coefficient to the non-pilot position of the OFDM symbol. In the third stage, another AR model is assumed to exploit the correlation among the inter-subbands followed by the LMMSE technique for the estimation.
    b) *Dual adaptive channel estimation (DACE):* We also apply an adaptive algorithm to reduce computational complexity based on the least mean square (LMS) approach. This is a two-level recursive one, where the first recursion loop is from the intra-subband and then the second one is from the inter-subbands. We call it the dual adaptive channel estimation (DACE) technique.

B. SECONDARY CONTRIBUTIONS

1) *THz environment aware precoder:* Spectrum in the higher part of the band faces stronger attenuation due to environment, wideband path loss, frequency-dependent scattering/reflection, etc. resulting in poor signal detection performance at the subcarrier present in this part of the band. We propose a precoder design in the frequency domain that mitigates the wideband effect in the THz channel, specifically the path loss and environment-related effect, and balances the overall gains across the wideband. This precoder takes feedback of transceiver distance, and environment-related parameters like temperature, air pressure, and compositions. It also takes into account low Doppler presence and distance estimation inaccuracy.
2) *Minimum bit error rate (MBER) based parameter design:*We have proposed the two parameters, i.e. the number of zero subcarriers and the number of subbands to be optimally determined based on the MBER criterion with the assured bit error rate (BER).
    a) *Zero-subcarrier reduction:* One of the key bottlenecks in the MB-OFDM system is the usage of various low pass and band pass filters, which increase the number of zero-subcarriers that reduce the spectral efficiency. We have adopted the MBER-based approach for obtaining

an optimal number of zero-padding subcarriers with respect to a target BER.

b) *Optimal subband number:* Another key aspect of the proposed THz system is the number of optimal subbands. We have adopted the MBER-based approach, where the number of subbands can be obtained for a target BER.

Notation: Bold upper and lower case letters denote matrix and vector, respectively. The superscripts $(\cdot)^T$ and $(\cdot)^H$ denote the transpose and conjugate of a matrix, respectively. $\mathbb{E}[\cdot]$ denotes the expectation, while $\mathbf{I}_N$ denotes $(N \times N)$-element identity matrix.

II. BACKGROUND: THZ CHANNEL OVERVIEW

An overview of the THz channel and the wideband filter bank channel model is given below.

A. FREQUENCY DEPENDENT MODEL OF THZ CHANNEL

The frequency response of the wideband THz channel at a particular time t is the superposition of frequency responses of the N_p multipaths at that time and is given as

$$H(f,t) = \sum_{i=1}^{N_p} H_i(f,t), \tag{1}$$

where the frequency response of the i^{th} multipath is given by

$$H_i(f,t) = |H_i(f,t)|e^{j\angle H_i(f,t)}. \tag{2}$$

In the conventional cellular bands, the magnitude response of the i^{th} path $|H_i(f,t)| = |H_i(t)|$ can be considered, i.e. independent of frequency, because of the small signal bandwidth. As the magnitude response $|H_i(t)|$ is flat across the whole bandwidth of interest, we can apply the linear phase criterion on each path and hence the total frequency response of the channel can be given as

$$H(f,t) = \sum_{i=1}^{N_p} |H_i(t)|e^{-j2\pi f\tau_i(t)}, \tag{3}$$

where $\tau_i(t)$ is the delay of the i^{th} multipath. Therefore, even though the individual attenuation and delays of the multipaths are assumed to be frequency-independent in conventional cellular bands, the frequency selectivity arises because of the different multipath delays on each paths. That is, a particular multipath structure results in a single frequency or impulse response for the entire bandwidth of interest. When the multipath structure changes with time, we have a different frequency or impulse response.

However in the THz band, the input signal bandwidth is huge and the magnitude response on each path is frequency-dependent, as it is the product of attenuation due to path loss, absorption loss, and phenomena-dependent loss. The phenomena-dependent loss could be reflection, scattering, or diffraction loss depending on the nature of the multipath. The magnitude response for the i^{th} path is as follows

$$|H_i(f,t)| = |H_i(f,t)^F| \times |H_i(f,t)^A| \times |H_i(f,t)^P|, \tag{4}$$

where $|H_i(f,t)^F|$ is the attenuation of the i^{th} path due to path loss, $|H_i(f,t)^A|$ is the attenuation on the i^{th} path due to molecular absorption loss and $|H_i(f,t)^P|$ is the phenomena dependent loss on the i^{th} path at time t. Assuming low Doppler, we remove the time notation. Hence, the attenuation due to path loss is given by [4]

$$|H_i(f)^F| = \frac{c}{4\pi f r_i}, \tag{5}$$

where c is the speed of light and r_i is the path length of the i^{th} path. The attenuation due to environmental absorption loss is given by [4]

$$|H_i(f)^A| = e^{-\frac{1}{2}k(f)r_i}, \tag{6}$$

where $k(f)$ is the frequency-dependent absorption coefficient as follows [4]

$$k(f) = \sum_q \frac{p}{p_0}\frac{T_0}{T}Q^q\sigma^q(f), \tag{7}$$

where p_0 is the reference pressure, T_0 is the reference temperature, p is the pressure, T is the temperature, Q^q is the number of molecules per unit volume of gas q and $\sigma^q(f)$ is the absorption cross section of gas q. Work in [4] shows that oxygen and water vapour affect the absorption coefficient the most and their approximate percentages in the air are obtained from sensors. The absorption cross sections of the gases depend on the line intensity and the line shape which are available in the HITRAN database [3]. Also, the reference air pressure is assumed to be 101325 pascals, which is a standard value at sea level. We plot the channel spectrum in FIGURE 1 as an example. We observe almost a 5 dB loss in spectrum gain within the $190 - 207$ GHz band.

The phenomena dependent loss $|H_i(f)^P|$ could be due to reflection, scattering, or diffraction depending on the nature of the surface, on which the i^{th} multipath falls. More details can be found in [4]. As a result of the above-mentioned propagation phenomena in the THz band, the various multipaths already have a frequency selectivity nature. Therefore, the THz wireless channel will have a frequency selectivity due to the random multipath delays on top of the already existing frequency-dependent nature of the individual multipaths due to molecular absorption and other frequency-dependent propagation phenomena. Hence, there is a need for an appropriate model that characterizes these effects in a simple and mathematically tractable way. This motivates the proposed filter bank channel model and the subsequent THz-specific MB-OFDM architecture as explained next.

B. BASEBAND INPUT-OUTPUT FILTER BANK CHANNEL MODEL

Hence, to simplify the THz channel model, the complete wideband is proposed to be split into M number of smaller subbands. The m^{th} subband will have the frequency response from the i^{th} path $H_i^m(f)$ as an all-pass filter. We ignore the Doppler effect for the time being. Therefore, the frequency

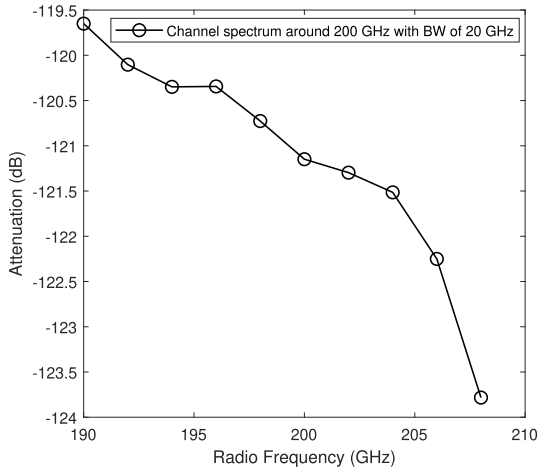

FIGURE 1. Plot of channel spectrum for 20 GHz bandwidth around 200 GHz central frequency.

response of the wideband THz channel is expressed as follows

$$H(f) = \sum_{m=1}^{M} H^m(f), \tag{8}$$

where $H^m(f)$ is the total channel spectrum at the m^{th} smaller band and can be expressed as

$$H^m(f) = \sum_{i=1}^{N_p} H_i^m(f). \tag{9}$$

Now (9) can be realized in the digital baseband domain using FIR filter, with the channel coefficients as follows [43]

$$\mathbf{h}_m^c = \left[h_{m,0}^c \; h_{m,1}^c \; \cdots \; h_{m,P-1}^c\right], \tag{10}$$

where $h_{m,i}^c$ represents the i^{th} discrete channel coefficient for the m^{th} subband and P is the total number of channel coefficients. Therefore, using (9) and (10), we can approximate the entire wideband THz channel as a parallel FIR filter bank where the filter coefficients remain approximately frequency-invariant across the smaller subbands. So, the transmitted waveform needs to be redesigned to fit the wideband THz channel model.

III. PROPOSED THZ-SPECIFIC MB-OFDM WAVEFORM DESIGN (TRANSMITTER PART)

We propose to use MB-OFDM based waveform in a wide THz band. As explained earlier, the wideband THz channel can be approximated as a filter bank with parallel narrowband FIR filters with approximately frequency-invariant filter coefficients. This enforces an appropriate waveform design. The proposed transmitted waveform for THz is designed to contain multiple independent narrow-band data, which are separated in the spectral domain from each other. We initially present the proposed waveform design for THz without beamforming for the ease of data model description. Subsequently, we describe the beamforming and receiver design.

The data model of the MB-OFDM waveform is conceived in multiple stages. The wide bandwidth of the input signal is first split into M number of smaller bands. The transmitter baseband architecture is shown in FIGURE 2a.

A. STAGE-1: MULTIPLE OFDM SYSTEMS

Let us assume that the total transmission bandwidth is B_t and we subdivide it into M smaller bands. Each band will have $N = \dfrac{B_t}{M\Delta f}$ subcarriers, where Δf is the subcarrier spacing in the frequency domain. Zero padding is carried out at the beginning and at the end of each subband to avoid interference between neighboring subbands. Let us assume that N_z denotes the number of zero subcarriers in a subband. It is also assumed that $N_z/2$ number of zeros will be added at the beginning and at the end of each band.

These zero subcarriers (N_z) act as a guard band against the filtering effect described later. Let us assume that the frequency domain symbol vector at the m^{th} subband including the zero padding is denoted as $\mathbf{s}^m \in \mathbb{C}^{N\times 1}$. The corresponding time-domain samples for the m^{th} subband after CP addition is denoted as $\mathbf{x}^m \in \mathbb{C}^{(N+L_c)\times 1}$, where L_c is the CP length, $\mathbf{x}^m[L_c+1:(N+L_c)] = \mathbf{F}^H\mathbf{s}^m$, $\mathbf{F}$ is the FFT matrix and $\mathbf{x}^m[1:L_c]$ is the CP sequence.

B. STAGE-2: UPSAMPLE AND INTERPOLATION FILTERING

At the next stage, the $\mathbf{x}^m$ sequence will be upsampled by the factor M and a new sequence $\mathbf{x}_1^m \in \mathbb{C}^{M(N+L_c)\times 1}$ is generated as follows

$$\begin{aligned} x_1^m[n] &= x^m[n/M], \text{ when } n \text{ is divisible by } M, \\ &= 0, \text{ otherwise.} \end{aligned} \tag{11}$$

The z-transform of $x_1^m[n]$ sequence is defined as

$$X_1^m(z) = X^m(z^{-M}), \tag{12}$$

where $X^m(z)$ is the z-transform of $\mathbf{x}^m$ and is defined as

$$X^m(z) = \frac{1}{\sqrt{N}} \sum_{l=0}^{N+L_c-1} \left[\sum_{n=0}^{N-1} e^{-j\omega ln/N} s^m[n]\right] z^{-l}. \tag{13}$$

Then, $X_1^m(z)$ is passed to a low pass filter (LPF) having transfer function $H_1(z)$, which has a normalized cut-off frequency of π/M. We assume that the LPF filter has a finite length of L_1. Hence, the z-transform of the resultant signal, $x_2^m[n]$ after filtering is

$$X_2^m(z) = X_1^m(z)H_1(z). \tag{14}$$

C. STAGE-3: ORTHOGONAL SPECTRUM SHIFTER AND COMBINER

In this stage, a band-shifting operation by multiples of π/M is performed on each of the individual band-limited time domain sequences so that each one of them is orthogonal in the spectral domain. Let us assume that the time domain

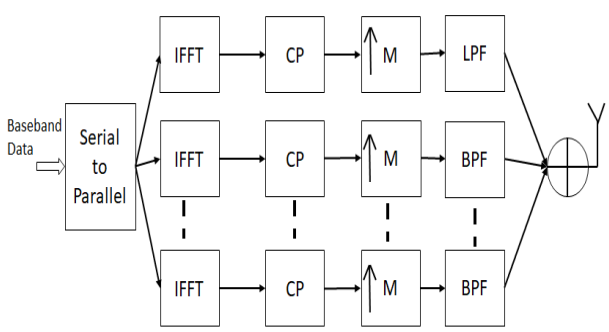

(a) Proposed Tx structure for the THz-specific MB-OFDM waveform generation (Excluding beamforming).

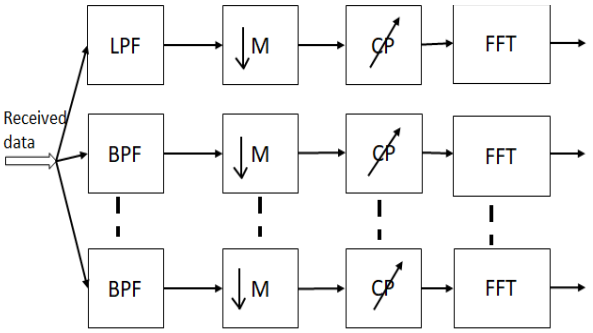

(b) Proposed Rx structure for the THz-specific MB-OFDM waveform (Excluding beamforming).

FIGURE 2. Proposed MB-OFDM waveform-based THz baseband transceiver design architecture.

sequence of the shifted spectrum of the m^{th} subband, i.e. $X_3^m(\omega) = X_2^m(\omega - \frac{m\pi}{M})$ is $x_3^m[n]$. The final step is the addition of all the information-carrying time domain sequences having an orthogonal spectrum to generate the single digital waveform sequence. Hence, the final digital transmitted waveform at the n^{th} discrete time with power normalization is as follows

$$x^t[n] = \frac{1}{\sqrt{M}} \sum_{m=1}^{M} x_3^m[n]. \tag{15}$$

1) FRONT-END FILTER BANK

The front-end filter bank plays a crucial role in an MB-OFDM THz system, enhancing its overall performance and reliability. These filters are responsible for managing the total bandwidth efficiently by splitting the available frequency spectrum into multiple smaller sub-bands. This partitioning along with the proposed waveform design allows MB-OFDM to transmit data simultaneously over different frequency bands, improving the system's capacity and robustness against interference. This spectral segmentation helps in controlling the signal's spectral characteristics, minimizing the leakage of energy into adjacent frequency bands, and thus reducing out-of-band emissions.

D. PEAK-TO-AVERAGE POWER RATIO (PAPR) APPROXIMATION

We analyze the PAPR of the proposed waveform now. Let NM be the total number of subcarriers in the conventional OFDM system and the proposed MB-OFDM, where N is the number of subcarriers in a subband within the proposed waveform design and M is the number of subbands. We use filter at every subband after upsampling by a factor of M. Following [16], [44], and [45], the complementary cumulative distribution function (CCDF) of the PAPR corresponding to the m^{th} subband sequence can be approximated as

$$Pr(PAPR^m \geq \gamma) \approx 1 - \prod_{n=0}^{NM-1} \left(1 - e^{-\frac{\gamma}{MN|h_{eff}(n-MN)|^2}}\right), \tag{16}$$

where $PAPR^m$ is the PAPR at the m^{th} subband, γ is the PAPR threshold and $h_{eff}(u)$ is the effective filter coefficient at every time sample and is defined as

$$h_{eff}(u) = \frac{1}{MN} \sum_{k=0}^{NM-1} \left[\sum_{l=0}^{L_1-1} h_l e^{-\frac{2\pi kl}{NM}}\right] e^{\frac{j2\pi uk}{MN}}, \tag{17}$$

where h_l is the l^{th} coefficient of L_1-length interpolation filter having transfer function $H_1(z)$ as defined earlier. From (15), we assume that each subband sequence is independent. Therefore, the overall CCDF is the multiplication of all individual CCDFs, when the sum of independent random variables is considered. Hence, we can obtain an approximate theoretical expression for the CCDF of PAPR of the final MB-OFDM waveform as

$$Pr(PAPR \geq \gamma) \approx \left(1 - \prod_{n=0}^{NM-1} (1 - e^{-\frac{\gamma}{MNh_{eff}^2(n-MN)}})\right)^M. \tag{18}$$

Note: The above bound is not tight and it exhibits inaccuracy. We take an opportunity to fine tune it as a future work. However, we continue to demonstrate this approximate result in later section.

IV. BEAMFORMING AND RECEIVER DESIGN

A. BEAMFORMING DESIGN

We consider a wideband THz system having N_t number of antennas at the transmitter (Tx) and N_r number of antennas at the receiver (Rx), respectively. The transmitter and receiver have only one RF chain. The beamforming at the transmitter and the combining at the receiver are implemented in the analog domain using digitally controlled phase shifters.

Ignoring the continuous time notion for simplicity, the transmitter uses the analog beamforming vector $\mathbf{f}_t$ to transmit the input signal $\mathbf{x}^t$ and the received signal is combined using the combining vector $\mathbf{z_r}$. We maintain that $\|\mathbf{z}_r\|^2 = 1$. Assuming a frequency selective channel, the baseband received signal $y[n]$ at the n^{th} discrete time after the combiner can be written as

$$y[n] = \sum_{p=0}^{P-1} \left[\mathbf{z}_r^H \mathbf{H}_p \mathbf{f}_t\right] x^t[n-p] + w[n], \tag{19}$$

where P is the number of channel taps in delay spread domain, $\mathbf{H}_p$ is the $N_r \times N_t$ wideband THz channel matrix considered at the p^{th} delay sample with high sampling rate and $w[n]$ is the additive white Gaussian noise (AWGN). As the THz channel can be assumed to be more sparser than a mmWave channel, we use the geometric channel model with a very small number of dominant paths L to characterize the THz channel. Therefore, the channel can be expressed as

$$\mathbf{H}_p = \sum_{m=1}^{M} \sum_{l=1}^{L} \alpha_{l,p}^m \mathbf{a_R}(\theta_l^r, \phi_l^r) \mathbf{a_T}^H(\theta_l^t, \phi_l^t), \tag{20}$$

where $\theta_l^t, \theta_l^r \in [0, \pi]$ and $\phi_l^t, \phi_l^r \in [-\pi, \pi]$ are the associated elevation angle and azimuth angles for both AoD and AoA. Similarly, $\mathbf{a_R}(\theta_l^r, \phi_l^r) \in \mathbb{C}^{N_r \times 1}$ and $\mathbf{a_T}(\theta_l^t, \phi_l^t) \in \mathbb{C}^{N_t \times 1}$ are the array response vectors associated with the l^{th} path in the receiver and transmitter, respectively and α_l^m is the path gain of the l^{th} path in the m^{th} subband. In the case of UPA, we can write $N_r = N_x^r \times N_y^r$ and $N_t = N_x^t \times N_y^t$, where N_x^r, N_y^r and N_x^t, N_y^t are antenna numbers in the x and y coordinates at the receiver and transmitter, respectively. The array response at the $(m, n)^{th}$ antenna element of the UPA configuration at the transmitter and receiver can be written as [27]

$$[\mathbf{a_T}(\theta_l^t, \phi_l^t)]_{m,n} = \exp\left[\frac{j2\pi}{\lambda} \tau_{m,n}^t\right], \tag{21}$$

where delay $\tau_{m,n}^t$ can be written as

$$\tau_{m,n}^t = (m-1)(n-1)d^2 \left[\sin(\theta_l^t)\cos(\phi_l^t) + \sin(\theta_l^t)\sin(\phi_l^t)\right], \tag{22}$$

where d is the distance between the two consecutive antenna elements. (21) and (22) can be extended for array response at the receiver as well. During the training phase, the transmitter uses P_1 number of pilot beam patterns $\mathbf{f}_t$ and the receiver uses P_2 number of pilot beams of $\mathbf{z}_r$. The transmitter successively emits the training beams $\{\mathbf{f}_t\}$ during the training period and at the receiver each training beam is received through its beam patterns $\{\mathbf{z}_r\}$. Hence, the training phase consists of $P_1 \times P_2$ combinations of beamformers and combiners. We choose a combination of beamformer and combiner, which produces the highest received signal-to-noise ratio (SNR) at the receiver.

B. RECEIVER DESIGN BASED ON THE PROPOSED WAVEFORM

Let us consider the general data model corresponding to the $(p, q)^{th}$ beamformer-combiner combination. Post-combiner, the data is still at the higher sampling rate with very wideband. A series of reverse operations with respect to the transmitter will follow now as shown in FIGURE 2b.

1) BAND PASS FILTERING

The first blocks are band pass filters (BPF), which can be implemented as shifting the desired subband to the baseband area followed by LPF. The frequency spectrum of the output sequence for the m^{th} subband will be as follows

$$Y^m(\omega) = Y\left(\omega + \frac{m\pi}{M}\right) H_2(\omega), \tag{23}$$

where $Y(\omega)$ and $H_2(\omega)$ are the frequency spectrum of (19) and an LPF having cutoff at π/M, respectively. Let us assume that the time domain sequence corresponding to $Y^m(\omega)$ is $y^m[n]$. The m^{th} subband has P taps with the p^{th} one as follows

$$h_{m,p}^c = \mathbf{z}_r^H \left[\sum_{l=1}^{L} \alpha_{l,p}^m \mathbf{a_R}(\theta_l^r, \phi_l^r) \mathbf{a_T}^H(\theta_l^t, \phi_l^t)\right] \mathbf{f}_t. \tag{24}$$

Therefore, from (24) and (10), we write the z-transform of $\mathbf{h}_m^c$ as $H_m^c(z) = \sum_{p=0}^{P-1} h_{m,p}^c z^{-p}$.

2) DOWN SAMPLING

The next step is the down sampling of the time domain sequence $y^m[n]$ by the factor M. Let us define $Y_d^m(\omega)$ as the spectrum for the down sampled sequence for the m^{th} subband. This is defined as follows

$$Y_d^m(\omega) = \frac{1}{M} \sum_{k=0}^{M-1} Y^m(e^{j(\omega - 2\pi k)/M}). \tag{25}$$

Let us assume that the time domain sequence of (25) after CP discarding is $y_d^m[n]$ for $n = 0, 1, \ldots, N-1$. Therefore, after the FFT operation at each subband, the discrete frequency domain sequence corresponding to the m^{th} subband is defined as

$$\mathbf{y}_d^m = \Sigma_d^m \mathbf{s}^m + \mathbf{w}^m, \tag{26}$$

where Σ_d^m is the diagonal matrix containing all the eigenvalues of the effective circular channel corresponding to the m^{th} subband. The n^{th} subcarrier of the m^{th} subband is detected using simple method as $\hat{s}^m[n] = \frac{y_d^m[n]}{\hat{e}_{m,n}}$ followed by constellation mapping, where $\hat{e}_{m,n}$ is the estimated eigenvalue.

Proposition 1: The n^{th} diagonal element of the Σ_d^m matrix after FFT operation is given as follows

$$e_{m,n} = \sum_{p=0}^{L_e-1} \exp(-j2\pi pn) \sum_{l=0}^{Mp} \left[\sum_{k=0}^{l} h_{1,k} h_{m,l-k}^c\right] h_{2,Mp-l}, \tag{27}$$

where L_e is the effective channel length after down sampling.

proof: Effectively, the system at each subband has three filters with high sampling rate. The key assumption here is that there is negligible interference from the neighboring subbands. We also assume that the shifter at the transmitter and the receiver are the same with only reverse direction of band shifting with respect to each other. Therefore, the effective channel with high sampling rate for the m^{th} subband is as follows

$$H_m^u(z) = H_1(z)H_m^c(z)H_2(z), \tag{28}$$

Let us assume that the filter coefficients of $H_1(z)$ are stacked in a vector as $\mathbf{h}_1 \in \mathbb{C}^{L_1\times 1}$. Similarly for $H_2(z)$, it is $\mathbf{h}_2 \in \mathbb{C}^{L_2\times 1}$ and $\mathbf{h}_m^c \in \mathbb{C}^{P\times 1}$ for $H_m^c(z)$. The total length of the effective channel filter is L_1+L_2+P. So (28) can be rewritten considering all the coefficients together as follows

$$H_m^u(z) = \sum_{j=0}^{L_1+P+L_2-1} z^{-j}\left[\sum_{l=0}^{j}\left[\sum_{k=0}^{l} h_{1,k}h_{m,l-k}^c\right]h_{2,j-l}\right]. \tag{29}$$

After down sampling by a factor M, the effective filter length will be $L_e \approx \lceil (L_1+P+L_2)/M \rceil$ and the transfer function will be as follows

$$H_m^d(z) = \sum_{p=0}^{L_e-1} z^{-Mp}h_m(Mp), \tag{30}$$

where $h_m(Mp)$ is the $(Mp)^{th}$ coefficient of $H_m^u(z)$ defined as follows

$$h_m(Mp) = \sum_{l=0}^{Mp}\left[\sum_{k=0}^{l} h_{1,k}h_{m,l-k}^c\right]h_{2,Mp-l}. \tag{31}$$

(30) is the equivalent down sampled channel for the individual m^{th} subband. This will form an $N \times N$ circular channel matrix after the CP cancellation. Now, after the FFT operation is performed, the channel matrix's n^{th} eigenvalues can be calculated as

$$e_{m,n} = \sum_{p=0}^{L_e-1} \exp\left(-j2\pi pn\right) h_m(Mp). \tag{32}$$

Using (31) in (32), we obtain (27). □

V. PROPOSED IMPAIRMENT AWARE SQUINT-EFFECT MODELLING AND MITIGATION IN THE DIGITAL DOMAIN

THz systems will be equipped with large antenna arrays for beamforming capabilities and will be handling ultra-wide bandwidth. This will result in the spatial wideband effect and the resulting beam squint problem when the delay spread across the array is larger than the sampling period. Therefore in addition to a THz-specific waveform, THz systems should be designed with simple and energy-efficient squint mitigation schemes. In this section, we propose a novel squint model and mitigation scheme within the digital domain for large antenna array wideband THz systems.

A. SQUINT EFFECT MODEL AS AN EQUIVALENT DELAY TAP CHANNEL IN BASEBAND

We model the impact of large antenna arrays on digital waveform by considering various impairments from PCB design to circuit imperfections and SFO resulting in an equivalent baseband digital model for the squint effect, thereby enabling efficient digital pre-processing using digital techniques to combat the squint effect. This innovative approach eliminates the need for costly and power-intensive TTDs in the analog domain, reducing both power consumption and hardware complexity. The impairment parameters are modelled as follows

1) The power amplifier (PA) to the antenna through the various PS till antenna points exhibits unequal transmission line length along with unequal delay. This length and delay will also have imperfections due to board design and fabrication imperfections. Let us assume that the RF modulated signal from the PA is $x_{RF}(t)$. Let us define that L_t, R_t, C_t, and G_t are the inductance, resistance, capacitance, and conductance per unit of transmission length from the PA to the antenna.
2) The expected length of PA to the $(m,n)^{th}$ antenna element through the PS is $l_{m,n}$. However, due to temperature variation and board design imperfection, the length can be approximated as $l_{m,n} + l_{m,n}\alpha_{as}\Delta T + \Delta l_{m,n}$. Here, we have introduced $\Delta l_{m,n}$ as a random imperfection in the length due to board design, α_{as} and ΔT are the thermal expansion coefficient of the metal and random temperature difference, respectively [46].
3) We consider that R_t depends on the temperature as $R_t = R_{t,o}\left[1+\alpha_t\Delta T\right]$, where $R_{t,o}$, α_t are resistance per unit length at the reference temperature and temperature coefficient of the conductor, respectively [47]. $R_{t,o}$ can be further defined as $R_{t,o} = \dfrac{\rho_o}{\pi a_w \delta_s}$, where ρ_o, a_w, δ_s are the resistivity at a reference temperature, cross-section area of conducting wire on PCB and skin depth, respectively. $\delta_s \approx \dfrac{503}{\sqrt{\mu_r f \sigma_c}}$, where μ_r, σ_c are the relative permeability and conductivity of metal [47] and f is the frequency.
4) We consider that the $(m,n)^{th}$ PS exhibits a base elevation angle of $(\theta_p + \Delta\theta_p^{m,n})$ and azimuth angle of $(\phi_p + \Delta\phi_p^{m,n})$, with $\Delta\theta_p^{m,n}$, $\Delta\phi_p^{m,n}$ being the random imperfections, respectively.
5) The array antenna positions will also have inaccuracies due to imperfections in board design. The distance between two consecutive antennas is $(d+\Delta d)$, where Δd is a random imperfection.

Therefore, considering all the above impairments, the overall antenna output in the UPA configuration $(N_x \times N_y)$ at a relative direction of (θ_p, ϕ_p) elevation and azimuth angles

can be written as follows

$$x^o_{RF}(t) = \sum_{n=1}^{N_x}\sum_{m=1}^{N_y} A_{m,n} x_{RF}(t-\delta_{m,n}), \tag{33}$$

where $A_{m,n}$ is the path gain from PA to antenna and $\delta_{m,n}$ is the path delay defined as follows

$$\delta_{m,n} = \left[\sqrt{L_t C_t}(l_{m,n} + l_{m,n}\alpha_{as}\Delta T)\right] + \frac{(m-1)(n-1)(d+\Delta d)}{c}\delta^A_{m,n}, \tag{34}$$

where $\delta^A_{m,n}$ is calculated considering the steering vector imperfection as

$$\begin{aligned}\delta^A_{m,n} &= \sin(\theta_p)\cos(\phi_p) + \sin(\theta_p)\sin(\phi_p) \\ &+ \Delta\theta_p^{m,n}\left[\cos(\theta_p)\cos(\phi_p) + \cos(\theta_p)\sin(\phi_p)\right] \\ &+ \Delta\phi_p^{m,n}\left[\sin(\theta_p)\cos(\phi_p) - \sin(\theta_p)\sin(\phi_p)\right].\end{aligned} \tag{35}$$

Now, $A_{m,n}$ is calculated as follows

$$A_{m,n} = \exp\left[-\frac{1}{2}\sqrt{L_t C_t}\left(\frac{R_t}{L_t} + \frac{G_t}{C_t}\right) l^a_{m,n}\right], \tag{36}$$

with $l^a_{m,n} \triangleq \left[l_{m,n}(1+\alpha_{as}\Delta T) + \Delta l_{m,n}\right]$. (36) can be further approximated as in (37), as shown at the bottom of the next page.

Now, (33) can be considered similar to the multi-ray signal reception model [43] and all these effects collectively can be modelled as an equivalent channel. Let us assume that the RF carrier frequency is f_c and the transmitter side DAC sampling clock period is $T_{DAC}(1+\eta)$, where η is the normalized SFO and T_{DAC} is the DAC sampling time without SFO. Then, the equivalent baseband discrete channel, which exists between the PA to the antennas, can be modelled for the p^{th} tap as viewed from the baseband side as follows [43]

$$\begin{aligned}h_{RF}[p] &= \sum_{n=1}^{N_x}\sum_{m=1}^{N_y} A_{m,n} e^{-j2\pi f_c \delta_{m,n}} \operatorname{sinc}\left(p - \frac{\delta_{m,n}}{T_{DAC}(1+\eta)}\right) \\ &\triangleq h^o_{RF}[p] + \epsilon_h[p],\end{aligned} \tag{38}$$

where $h^o_{RF}[p]$ is the impairment-free part, and $\epsilon_h[p]$ is the effective impairment in the p^{th} squint channel tap. We now approximate the $e^{-j2\pi f_c \delta_{m,n}}$ as in (40), as shown at the bottom of the next page. For approximating the "sinc" function in (38), we assume that the small impairments will not change its envelope value significantly. Let us define $C_{m,n,p} \triangleq \left(p - \frac{\delta^o_{m,n}}{T_{DAC}(1+\eta)}\right)$ and $\delta^o_{m,n} \triangleq \left[\sqrt{L_t C_t} l_{m,n} + \frac{(m-1)(n-1)d}{c}\left(\sin(\theta_p)(\cos(\phi_p)+\sin(\phi_p))\right)\right]$.

Therefore, we can approximate the following

$$\begin{aligned}\operatorname{sinc}\left(C_{m,n,p}\right) &= \frac{\sin\pi\left(p - \frac{\delta^o_{m,n}}{T_{DAC}}\right)}{\pi\left(p - \frac{\delta^o_{m,n}}{T_{DAC}(1+\eta)}\right)} \\ &\overset{(a)}{\approx} \frac{\sin\pi\left(p - \frac{\delta^o_{m,n}}{T_{DAC}}\right)}{\pi\left(p - \frac{\delta^o_{m,n}(1-\eta)}{T_{DAC}}\right)} \\ &\overset{(b)}{\approx} \underbrace{\operatorname{sinc}\left(p - \frac{\delta^o_{m,n}}{T_{DAC}}\right)}_{C^o_{m,n,p}} - \underbrace{\eta\frac{\operatorname{sinc}\left(p - \frac{\delta^o_{m,n}}{T_{DAC}}\right)}{\left(p - \frac{\delta^o_{m,n}}{T_{DAC}}\right)T_{DAC}}}_{C^\epsilon_{m,n,p}},\end{aligned} \tag{39}$$

where (a) is obtained by $\frac{1}{1+\eta} \approx (1-\eta)$ and (b) is obtained by approximating the denominator in a similar way as in (a). Hence, $h^o_{RF}[p]$ can be modelled as follows

$$h^o_{RF}[p] = \sum_{n=1}^{N_x}\sum_{m=1}^{N_y} A^o_{m,n} B^o_{m,n} C^o_{m,n,p}, \tag{41}$$

where $A^o_{m,n}$, $A^\epsilon_{m,n}$ are defined in (37), $B^o_{m,n}$, $B^\epsilon_{m,n}$ are defined in (40) and $C^o_{m,n,p}$, $C^\epsilon_{m,n,p}$ are defined in (39). Similarly, the impairment $\epsilon_h[p]$ can be modelled as in (42), as shown at the bottom of the next page,

The variance of $\epsilon_h[p]$, i.e σ^2_ϵ can be calculated as in (43), as shown at the bottom of page 11.

Note: It is noted from (38) that the p^{th} tap due to the squint effect has noise component due to several impairments as mentioned earlier. In case, the statistics are not available, then they can be discarded, and non-Bayesian based solution for compensation can be framed.

B. SQUINT MITIGATION FILTER DESIGN

The design of the squint mitigation filter, utilizing the squint model from (38), can be conducted with or without accounting for the noise component. Let us assume that the equivalent squint effect channel has length K_1. Now if we ignore the error part, i.e $\epsilon_h[p]$, then the digital mitigation filter $H_s(z)$ is a simple inversion of the FIR filter $\mathbf{h}^o_{RF} = \left[h^o_{RF}[0]\ h^o_{RF}[1]\ldots h^o_{RF}[K_1-1]\right]^T$ consisting of channel taps $h^o_{RF}[p]$ as follows

$$H_s(z) = \frac{1}{\sum_{p=0}^{K_1-1} h^o_{RF}[p] z^{-p}}. \tag{44}$$

The implementation of the mitigation filter $H_s(z)$ can be achieved using the FIR filter by employing the standard infinite impulse response (IIR) to FIR techniques.

The LMMSE-based technique is adopted for the digital squint mitigation filter design considering the noise part $\epsilon_h[p]$. Let us assume that the squint mitigation filter coefficients are defined as $\mathbf{h}_s \in \mathbb{C}^{K_2\times 1}$ having order

K_2. Then the optimization problem can be formulated as follows

$$\arg\min_{\mathbf{h}_s} \mathbb{E}\|x^t[p] - (\mathbf{h}_{RF}^o)^H \mathbf{X}^t \mathbf{h}_s - (\boldsymbol{\epsilon}_h)^H \mathbf{X}^t \mathbf{h}_s\|^2, \quad (45)$$

where $\mathbf{X}^t \in \mathbb{C}^{K_1 \times K_2}$ is a matrix containing the pre-filtering transmitted signal $\mathbf{x}^t$ from (15). (45) has a standard solution as given by (skipping the standard derivation)

$$[\mathbf{h}_s]^H = \sigma_x^2 (\mathbf{I}_1 \mathbf{h}_{RF}^o)^H \left[(\mathbf{I}_1 \mathbf{h}_{RF}^o)(\mathbf{I}_1 \mathbf{h}_{RF}^o)^H \sigma_x^2 + \sigma_\epsilon^2 \mathbf{I} \right]^{-1}. \quad (46)$$

with σ_x^2 being the power spectral density of $x^t[n]$ and $\mathbf{I}_1 \in \mathbb{R}^{K_2 \times K_1}$ is a matrix with entry 1 or 0.

$$\begin{aligned}
A_{m,n} &\approx \exp\left[-\frac{1}{2}\sqrt{L_t C_t}\left(\frac{R_{t,o}}{L_t} + \frac{G_t}{C_t}\right) l_{m,n}\right] \\
&\quad \times \exp\left[-\frac{1}{2}\sqrt{L_t C_t}\left(\frac{R_{t,o}}{L_t} + \frac{G_t}{C_t}\right) \frac{l_{m,n}^2 \alpha_t \Delta T R_{t,o}}{L}\left(\alpha_{as}\Delta T + \frac{\Delta l_{m,n}}{l_{m,n}}\right)\left(1 + \alpha_{as}\Delta T + \frac{\Delta l_{m,n}}{l_{m,n}}\right)\right], \\
&= \exp\left[-\frac{1}{2}\sqrt{L_t C_t}\left(\frac{R_{t,o}}{L_t} + \frac{G_t}{C_t}\right) l_{m,n}\right] \exp\left[-\left(\frac{R_{t,o}}{L_t} + \frac{G_t}{C_t}\right) \frac{\sqrt{L_t C_t} l_{m,n}^2 \alpha_t \Delta T R_{t,o}}{2L}\left(\alpha_{as}\Delta T + \frac{\Delta l_{m,n}}{l_{m,n}} + \frac{2\alpha_{as}\Delta T \Delta l_{m,n}}{l_{m,n}}\right)\right], \\
&\overset{(a)}{\approx} \underbrace{\exp\left[-\frac{1}{2}\sqrt{L_t C_t}\left(\frac{R_{t,o}}{L_t} + \frac{G_t}{C_t}\right) l_{m,n}\right]}_{A_{m,n}^o} \\
&\quad + \underbrace{\exp\left[-\frac{1}{2}\sqrt{L_t C_t}\left(\frac{R_{t,o}}{L_t} + \frac{G_t}{C_t}\right) l_{m,n}\right]\left[\left(\frac{R_{t,o}}{L_t} + \frac{G_t}{C_t}\right) \frac{\sqrt{L_t C_t} l_{m,n}^2 \alpha_t \Delta T R_{t,o}}{2L}\left(\alpha_{as}\Delta T + \frac{\Delta l_{m,n}}{l_{m,n}} + \frac{2\alpha_{as}\Delta T \Delta l_{m,n}}{l_{m,n}}\right)\right]}_{A_{m,n}^\epsilon},
\end{aligned} \quad (37)$$

where (a) is obtained by ignoring $(\Delta T)^2$ and $(\Delta l_{m,n})^2$ and expanding the second exponential as $\exp(x) \approx 1 - x$.

$$\begin{aligned}
e^{-j2\pi f_c \delta_{m,n}} &= \exp\left[-2\pi f_c \left[\sqrt{L_t C_t} l_{m,n} + \sqrt{L_t C_t} l_{m,n} \alpha_t \Delta T + \frac{(m-1)(n-1)(d+\Delta d)}{c} \delta_{m,n}^A\right]\right] \\
&= \exp\left(-j\left[2\pi f_c \sqrt{L_t C_t} l_{m,n} + D_{m,n}\left(\sin\theta_p \cos\phi_p + \sin\theta_p \sin\phi_p\right) d\right]\right) \\
&\quad \times \exp\left(-j\left[C_{m,n}^\epsilon + D_{m,n}\left[d\Delta\theta_p^{m,n}\left(\cos\theta_p \cos\phi_p + \cos\theta_p \sin\phi_p\right)\right]\right]\right) \\
&\quad \times \exp\left(-j\left[D_{m,n}\left[d\Delta\phi_p^{m,n}\left(\sin\theta_p \cos\phi_p - \sin\theta_p \sin\phi_p\right) + \delta_{m,n}^A \Delta d\right]\right]\right) \\
&\overset{(a)}{\approx} \underbrace{\exp\left(-j\left[2\pi f_c \sqrt{L_t C_t} l_{m,n} + D_{m,n}\left(\sin\theta_p \cos\phi_p + \sin\theta_p \sin\phi_p\right) d\right]\right)}_{B_{m,n}^o} \\
&\quad + j\left[C_{m,n}^\epsilon \Delta T + D_{m,n}\left[d\Delta\theta_p^{m,n}\left(\cos\theta_p \cos\phi_p + \cos\theta_p \sin\phi_p\right) + d\Delta\phi_p^{m,n}\left(\sin\theta_p \cos\phi_p - \sin\theta_p \sin\phi_p\right) + \delta_{m,n}^A \Delta d\right]\right], \\
&\quad \underbrace{\times \exp\left(-j\left[2\pi f_c \sqrt{L_t C_t} l_{m,n} + D_{m,n}\left(\sin\theta_p \cos\phi_p + \sin\theta_p \sin\phi_p\right) d\right]\right)}_{B_{m,n}^\epsilon}
\end{aligned} \quad (40)$$

where $C_{m,n}^\epsilon \triangleq 2\pi f_c \sqrt{L_t C_t} l_{m,n} \alpha_t$ and $D_{m,n} \triangleq \frac{2\pi(m-1)(n-1)}{\lambda}$ and (a) is approximated using $\exp(x) \approx 1 - x$.

$$\begin{aligned}
\epsilon_h[p] &= \sum_{n=1}^{N_x} \sum_{m=1}^{N_y} A_{m,n}^o \left(B_{m,n}^o C_{m,n,p}^\epsilon + B_{m,n}^\epsilon \left(C_{m,n,p}^o + C_{m,n,p}^\epsilon\right)\right) + A_{m,n}^\epsilon \left(B_{m,n}^o + B_{m,n}^\epsilon\right)\left(C_{m,n,p}^o + C_{m,n,p}^\epsilon\right) \\
&\overset{(a)}{\approx} \sum_{n=1}^{N_x} \sum_{m=1}^{N_y} \left[A_{m,n}^o B_{m,n}^o C_{m,n,p}^\epsilon + A_{m,n}^o B_{m,n}^\epsilon C_{m,n,p}^o + A_{m,n}^\epsilon B_{m,n}^o C_{m,n,p}^o\right],
\end{aligned} \quad (42)$$

where (a) is obtained by ignoring multiplications of small errors like $B_{m,n}^\epsilon C_{m,n,p}^\epsilon$.

VI. PROPOSED THZ CHANNEL ESTIMATION

We have proposed a channel estimation based on the post-FFT i.e. frequency domain data in this MB-OFDM context. We propose a bandwise channel estimation in the frequency domain for each subband. The channel is estimated for each subband and subcarrier individually. To enhance the accuracy and efficiency of channel estimation, we exploit the existence of inter-dependencies and correlations among subbands in the frequency domain. In the proposed MB-OFDM architecture, post-FFT data is used for channel estimation, primarily because this data will make the individual subband's frequency domain channel matrix as a diagonal one [48], [49], [50] and estimation becomes relatively low complex. However, the above works did not exploit the sparsity. Though recent work in [51] uses pre-FFT (time-domain) data exploiting the sparsity for parameter estimation, it does not exploit the inter and intra-subband correlation. However, in this work, one of the key aspects of channel estimation is the exploitation of the inter and intra-subband correlations, which can be well captured in the frequency domain. We apply a three-stage channel estimation technique with the exploitation of the intra-subband and inter-subband frequency correlation. During the initial stage, we employ an LS-based algorithm for channel estimation, focusing on determining the channel coefficients in the frequency domain aligned with the pilot positions. Subsequently, in the second stage, we assume an AR model, leveraging intra-subband correlation. Here, we apply the LMMSE technique to estimate channel coefficients for non-pilot positions within the OFDM symbol. In the third stage, we assume another AR model to exploit inter-subband correlation, followed by the application of the LMMSE technique for estimation.

1) LMMSE BASED CHANNEL ESTIMATION

The channel estimation is conceived from (26), as we need to estimate only the $M(N-N_z)$ eigenvalues of the channel. A non-Bayesian method of estimation of the channel is as follows

$$\hat{e}_{m,n} = \frac{y_d^m[n]}{s^m[n]}, \tag{47}$$

while $s^m[n]$ is the pilot at the n^{th} subcarrier of the m^{th} subband. We adopt a three-stage method to estimate the eigenvalues. In the first stage, (47) is used to estimate the eigenvalues corresponding to the pilot positions. We exploit the inter and intra-subband frequency domain correlation to estimate the rest of the eigenvalues of the channel matrix. Let us define $\hat{\mathbf{e}}_m^p$ as the estimated set of channel eigenvalues corresponding to the pilot positions as obtained from (47). In the second stage, an AR model is assumed for the rest of the eigenvalues as follows

$$e_{m,n} = \sum_{k=1, i_k \neq n}^{K} b_{m,n}^k e_{m,i_k} + v_1(n), \tag{48}$$

where K is the number of pilots in a subband and $i_1, i_2, \ldots, i_K$ are the set of indices containing pilots, $v_1(n)$ is an AWGN process with zero mean and $\sigma_{v_1}^2$ as variance and $b_{m,n}^k$ are linear coefficients. In the third stage, we assume that inter-subband correlation is contributed from the $(m-1)^{th}$ and $(m+1)^{th}$ subbands for the m^{th} one. A tentative AR model is assumed as follows

$$e_{m,n} = a_{m,n}^1 e_{m+1,n} + a_{m,n}^2 e_{m-1,n} + v_2(n), \tag{49}$$

where $a_{m,n}^1, a_{m,n}^1$ are two coefficients, $v_2(n)$ is an AWGN process with zero mean and $\sigma_{v_2}^2$ as variance. Pilots are equispaced having $(M_p - 1)$ number of zeros between any adjacent pilot pair. To avoid larger complexity in estimation for the second stage, an interpolation filter having a cut-off frequency of π/M_p is used. Effectively, M_p can be thought of as an upsample factor. In the second stage, we obtain the equalizer for the n^{th} subcarrier based on the LMMSE criterion as follows

$$\left[\mathbf{w}_n^1\right]^H = \mathbf{R}_{1,n}\mathbf{R}_2^{-1}, \tag{50}$$

where $\mathbf{R}_{1,n} \in \mathbb{C}^{1\times K} = \left[b_{m,n}^1, b_{m,n}^2, \ldots, b_{m,n}^K\right]$ and $\mathbf{R}_2 \in \mathbb{C}^{K\times K}$ is defined as follows

$$\mathbf{R}_2 = \begin{bmatrix} \sigma_e^2 & \sigma_{1,2} & \ldots & \sigma_{1,K} \\ \sigma_{1,2} & \sigma_e^2 & \ldots & \sigma_{2,K} \\ . & . & . & . \\ \sigma_{1,K} & \sigma_{2,K} & \ldots & \sigma_{K,K} \end{bmatrix} + \sigma_{v_1}^2 \mathbf{I}_K,$$

$$\begin{aligned}\sigma_\epsilon^2 = \sigma_\eta^2 \sum_{n=1}^{N_x}\sum_{m=1}^{N_y} (A_{m,n}^o B_{m,n}^o)^2 \left[\frac{\operatorname{sinc}\left(p - \frac{\delta_{m,n}^o}{T_{DAC}}\right)}{\left(p - \frac{\delta_{m,n}^o}{T_{DAC}}\right) T_{DAC}}\right]^2 \\ + \sum_{n=1}^{N_x}\sum_{m=1}^{N_y} \left(A_{m,n}^o C_{m,n,p}^o\right)^2 \left[\sigma_{\Delta T}^2 (C_{m,n}^\epsilon)^2 + (D_{m,n})^2 d^2 \sigma_a^2 \left(1 + 2\cos(\phi_p)\sin(\phi_p)\cos(2\theta_p)\right)\right] \\ + \sum_{n=1}^{N_x}\sum_{m=1}^{N_y} \left(B_{m,n}^o C_{m,n,p}^o\right)^2 \exp\left[-\sqrt{L_t C_t}\left(\frac{R_{t,o}}{L_t} + \frac{G_t}{C_t}\right) l_{m,n}\right] \left[\left(\frac{R_{t,o}}{L_t} + \frac{G_t}{C_t}\right)^2 \frac{L_t C_t l_{m,n}^4 \alpha_t^2 R_{t,o}^2 \sigma_{\Delta T}^2}{4L^2} \left(\alpha_{as}^2 \sigma_{\Delta T}^2 + \frac{\sigma_l^2}{l_{m,n}^2}\right)\right].\end{aligned} \tag{43}$$

where σ_e^2 is the power spectral density of each eigenvalue and $\sigma_{i,j}$ is the correlation between $e_{m,i}$ and $e_{m,j}$. The estimated new eigenvalues corresponding to the non-pilot positions are given as follows

$$\hat{e}^1_{m,n} = \left[\mathbf{w}^1_n\right]^H \hat{\mathbf{e}}^p_m. \tag{51}$$

In the third stage, we tune the estimated channel eigenvalue using the inter-subbands correlation. Let us stack the estimated eigenvalues using (51) for other subbands as $\hat{\mathbf{e}}^2_m = [\hat{e}^1_{m-1,n}\ \hat{e}^1_{m,n}\ \hat{e}^1_{m+1,n}]^T$. The equalizer is designed as follows

$$[\mathbf{w}^2_n]^H = \mathbf{R}_{n,3}\mathbf{R}_4^{-1}, \tag{52}$$

where $\mathbf{R}_{n,3} \in \mathbb{C}^{1\times 3} = \left[a^1_{m,n}, \sigma_e^2, a^2_{m,n}\right]$ and $\mathbf{R}_4 \in \mathbb{C}^{3\times 3}$ is defined as follows

$$\mathbf{R}_4 = \begin{bmatrix} \sigma_e^2 & a^1_{m,n} & 0 \\ a^1_{m,n} & \sigma_e^2 & a^2_{m,n} \\ 0 & a^2_{m,n} & \sigma_e^2 \end{bmatrix} + \sigma^2_{v_2}\mathbf{I}_3.$$

We ignore the correlation between $\hat{e}_{m+1,n}$ and $\hat{e}_{m-1,n}$. Therefore, the final estimated channel eigenvalue corresponding to the n^{th} index is $\hat{e}^2_{m,n} = [\mathbf{w}^2_n]^H\hat{\mathbf{e}}^2_m$. The overall algorithm is given in Algorithm 1.

2) DUAL ADAPTIVE CHANNEL ESTIMATION (DACE) ALGORITHM

The correlation coefficients in (48) and (49) are difficult to obtain. To address this issue and reduce computational complexity, we employ an adaptive algorithm, specifically the LMS-based approach. This approach operates on a two-level recursive structure where the first recursion loop is within the intra-subband, followed by the second one in the inter-subbands, as previously discussed. The equalizer from the first loop for the j^{th} iteration is given as follows

$$\mathbf{w}_n(j) = \mathbf{w}_n(j-1) + \mu\hat{\mathbf{e}}^p_m\epsilon_n(j-1), \tag{53}$$

where $\epsilon_n(j-1)$ is an error and is defined as $\epsilon_n(j-1) = e_r - [\mathbf{w}_n(j-1)]^H\hat{\mathbf{e}}^p_m$ with $e_r = \mathbf{w}_n(j)^H\hat{\mathbf{e}}^p_m$. The initial value of $\mathbf{w}_n(0)$ is taken to be a vector with unit value at the n^{th} position and zeros at the rest. Vector $\hat{\mathbf{e}}^2_m$ is formed as shown earlier and the second loop starts for the inter-subband correlation in a similar way as described in (53) for the j^{th} iteration as follows

$$\mathbf{w}_m(j) = \mathbf{w}_m(j-1) + \mu\hat{\mathbf{e}}^2_m\epsilon_m(j-1), \tag{54}$$

where the error component $\epsilon_m(j-1) = e_d - \mathbf{w}_m(j-1)\hat{\mathbf{e}}^2_m$ and $e_d = [\mathbf{w}_m(j)]^H\hat{\mathbf{e}}^2_m$. Both loops will exit if the error $\epsilon_n(j-1) \le \epsilon_{th}$ or $\epsilon_m(j-1) \le \epsilon_{th}$, where ϵ_{th} is the threshold. We now summarize the overall channel eigenvalue estimation solution in Algorithm 2.

a: REMARKS ON COMPLEXITY

As evident from Algorithm 1, there will be matrix inversion of size $K\times K$ and 3×3. Ignoring the second one, the complexity can be upper bounded as $\mathcal{O}(K^3)$. However, we notice that the Algorithm 2 requires a complexity in the order of $\mathcal{O}(K)$.

We also analyze the MB-OFDM structural complexity here. The N-point IFFT with radix-2 structure needs $(N^2 - N)$ and $(N^2/2 + N/2)$ number of additions and multiplications, respectively. The front-end filters after the upsampling having finite length of L_1 taps need $(L_1 - 1)$ additions and L_1 multiplications. Additionally, if the squint mitigation filter is deployed with FIR structure with K_2 taps, then $(K_2 - 1)$ additions and K_2 multiplications are required. Therefore, the total complexity in either transmitter or receiver with M subbands will be $M\left[\frac{3N^2}{2} - \frac{N}{2} + 2L_1 + 2K_2 - 2\right]$.

Algorithm 1 : LMMSE Based Channel Estimation

INPUT : $\mathbf{r}_{\mathrm{d}}^{\mathrm{m,n}}$, $\mathbf{R}_{1,\mathrm{n}}$, $\mathbf{R}_2$, $\mathbf{R}_{3,\mathrm{n}}$, $\mathbf{R}_4$
Step $-$ 1 :
for $n \in$ [Indices of pilots] **do**
  $\tilde{e}_{m,n} = \frac{r^m_d[n]}{s^m[n]}$.
end for
$\hat{\mathbf{e}}^p_m$ = Stack of all $\tilde{e}_{m,n}$.
Step $-$ 2, Step $-$ 3 :
for $n = 1$ to N **do**
  $[\mathbf{w}^1_n]^H = \mathbf{R}_{1,n}\mathbf{R}_2^{-1}$.
  $\hat{e}^1_{m,n} = \left[\mathbf{w}^1_n\right]^H\hat{\mathbf{e}}^p_m$
  $\mathbf{e}^2_m = [\hat{e}^1_{m-1,n}\ \hat{e}^1_{m,n}\ \hat{e}^1_{m+1,n}]$
  $\mathbf{w}^2_n = \mathbf{R}_{3,n}\mathbf{R}_4^{-1}$
  $\hat{e}^2_{m,n} = \left[\mathbf{w}^2_n\right]^H\mathbf{e}^2_m$.
  Assign: $\hat{e}_{m,n} = \hat{e}^2_{m,n}$
end for
RETURN : $\hat{e}_{m,n}$ as the final channel values

VII. PROPOSED PRECODER FOR ENVIRONMENT AND WIDEBAND PATH LOSS EFFECT MITIGATION

We propose a precoder which directly compensates the environmental and wideband path loss effect to a large extent. The precoder is a gain compensation at the subcarrier level of OFDM. From (4), it can be noted that the gains are frequency-sensitive. The key assumptions are as follows

1) The transmitter has distance measurement information between the Tx-Rx through various distinguishable/resolvable multipaths after the ADC sampling.
2) We consider that there will be error in distance measurement. We also assume that there exists a very low Doppler, which will add further uncertainty to the distance. These two components are assumed to be independent, having zero mean and total variance of σ_d^2.
3) We assume that the wideband effect is very low throughout the subband. Therefore, we need to determine only the M number of unique gains, i.e. for each subband. Therefore, all the subcarriers of a subband will be multiplied with the same gain. We also ignore any common gain factors across all subbands i.e. antenna gains etc. in the precoder gain calculation,

Algorithm 2 : Proposed DACE Algorithm

INPUT : $\hat{\mathbf{e}}_{\mathrm{mp,K_l}}$
for $n = 1$ to N **do**
  if n is not a pilot index **then**
    INITIAL :$\mathbf{w}_n(0), e_r = [\mathbf{w}_m(0)]^H \hat{\mathbf{e}}_m^p$
    for $j = 1$ to K_l **do**
      $\epsilon_n(j-1) = e_r - [\mathbf{w}_n(j-1)]^H \hat{\mathbf{e}}_m^p$
      if $\epsilon_n(j-1) \leq \epsilon_{th}$ **then**
        EXIT
      else
        $\mathbf{w}_n(j) = \mathbf{w}_n(j-1) + \mu \hat{\mathbf{e}}_m^p \epsilon_n(j-1)$
        $e_r = [\mathbf{w}_m(j)]^H \hat{\mathbf{e}}_m^p$
      end if
    end for
    Estimate: $\hat{e}_{m,n} \approx [\mathbf{w}_n(j)]^* \hat{\mathbf{e}}_m^p$
  end if
  $\hat{\mathbf{e}}_m^2 = [\hat{e}_{(m-1),n},\ \hat{e}_{m,n},\ \hat{e}_{(m+1),n}]^T$
  INITIAL :$\mathbf{w}^m(0), e_d = \hat{e}_{m,n}$
  for $j = 1$ to K_l **do**
    $\epsilon_m(j-1) = e_d - [\mathbf{w}_m(j-1)]^H \hat{\mathbf{e}}_m^2$
    if $\epsilon_n(j-1) \leq \epsilon_{th}$ **then**
      EXIT
    else
      $\mathbf{w}_m(j) = \mathbf{w}_m(j-1) + \mu \mathbf{e}^m \epsilon_m(j-1)$
      $e_d = [\mathbf{w}_m(j)]^H \hat{\mathbf{e}}_m^2$
    end if
  end for
  Estimate: $\hat{e}_{m,n} = e_d$
end for
RETURN : $\hat{e}_{m,n}$ as the final channel values

as they are compensated in the Rx LNA (low noise amplifier).

4) We could not compensate the attenuation due to scattering/reflection, as it is impossible to find the exact objects and their frequency-dependent scattering/reflection coefficients. So, the proposed gain compensation is for the environment and wideband path loss parts.

We also plot the effect of the attenuation constant with respect to the frequency subband and subcarriers in FIGURE 3. We observe that the attenuation constant is large at the larger radio frequency.

Assume that the precoding gain at the m^{th} subband is β_m and the uncertainty in distance due to measurement and low Doppler is Δr_i and the measured distance is $\hat{r}_i$ for the i^{th} resolvable path after the ADC sampling. Our key goal is to ensure that, after precoding gain multiplication, the individual subband gain, along with path loss and other environment-related gain loss, will be nearly equal. Therefore, the power gain of each subband after normalization,

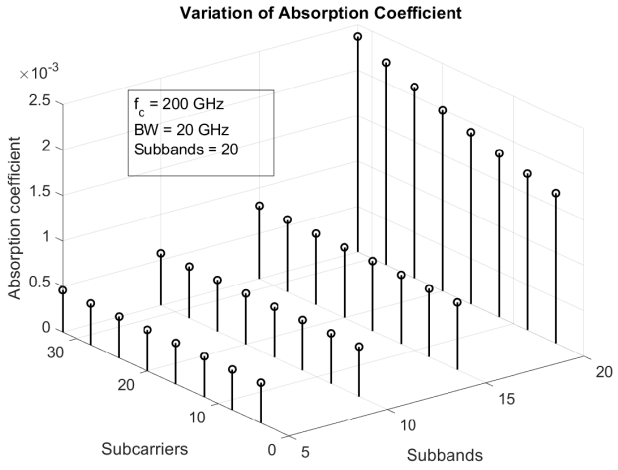

FIGURE 3. 3D-plot of the attenuation vs. spectrum is shown around the 200 GHz radio frequency.

which is expected to be almost one is defined as follows

$$\beta_m^2 \mathbb{E} \sum_{i=1}^{P_1} [K_i]^2 = 1, \tag{55}$$

where K_i is the path gain for the i^{th} path contributed by the path loss and environmental model only (excluding common multiplicative factors like antenna, LNA gains, and scattering/reflection, etc.), and it is defined as

$$K_i \triangleq \frac{\lambda_m}{\hat{r}_i + \Delta r_i} \exp\left(-\frac{1}{2} k(f_m)(\hat{r}_i + \Delta r_i)\right), \tag{56}$$

where f_m is the equivalent RF frequency value at the m^{th} subband center point and $\lambda_m = c/f_m$. K_i can be further approximated as follows

$$\begin{aligned} K_i &= \frac{\lambda_m}{\hat{r}_i} \left[\frac{1}{1 + \frac{\Delta r_i}{\hat{r}_i}} \exp\left[-\frac{1}{2} k(f_m)(\hat{r}_i + \Delta r_i)\right] \right] \\ &\overset{(a)}{\approx} \frac{\lambda_m}{\hat{r}_i} \left[\left(1 - \frac{\Delta r_i}{\hat{r}_i}\right) \exp\left[-\frac{1}{2} k(f_m)(\hat{r}_i + \Delta r_i)\right] \right] \\ &\overset{(b)}{\approx} \underbrace{\frac{\lambda_m}{\hat{r}_i} \exp\left[-\frac{1}{2} k(f_m)\hat{r}_i\right]}_{F_i} \left[1 - \underbrace{\left(\frac{1}{\hat{r}_i} + \frac{k(f_m)}{2}\right)}_{F_i^1} \Delta r_i \right] \\ &\triangleq F_i \left[1 - F_i^1 \Delta r_i\right], \end{aligned} \tag{57}$$

where (a) is obtained by approximating $\frac{1}{1 + \frac{\Delta r_i}{\hat{r}_i}} \approx \left(1 - \frac{\Delta r_i}{\hat{r}_i}\right)$, while for (b), we have applied $\exp(x) \approx 1 - x$.

Therefore, we can write as

$$\beta_m = \sqrt{\frac{1}{\mathbb{E}\sum_{i=1}^{P_1}\left[F_i[1-F_i^1\Delta d_i]\right]^2}} = \sqrt{\frac{1}{\sum_{i=1}^{P_1}(F_i)^2(1+(F_i^1)^2\sigma_d^2)}}, \tag{58}$$

where F_i and F_i^1 are defined in (57).

VIII. PROPOSED MBER-BASED OPTIMAL NUMBER OF SUB-BANDS AND ZERO-SUBCARRIERS

In this section, we discuss the proposed method using the MBER criterion to determine the optimal number of sub-bands and zero-padding subcarriers.

A. CHOICE OF ZERO SUBCARRIERS IN A SUBBAND

Let us assume that the number of zeros is N_z. We need to choose zeros in subcarriers to avoid intra-subband as well as inter-subband distortion. Intra-subband distortion arises due to the roll-off in any filter. We adopt a BER-based approach to determine N_z. We may use symbol error rate (SER) and BER interchangeably with the abuse of notation. This is because BER $\approx$ SER/$\log_2(M_1)$ at higher SNR, where M_1 is the constellation size.

Let us determine the inter-subband interference here. We assume here that such interference is possible only between consecutive bands. Therefore, the pre-FFT received signal's spectrum for the m^{th} subband can be expressed in (60), as shown at the bottom of the next page. We now consider that the interference at the m^{th} subband is due to the $(m-1)^{th}$ and $(m+1)^{th}$ subbands. We approximate (60) and obtain (61), as shown at the bottom of the next page, with uniform frequency sampling in $0 \le \omega \le 2\pi$. After discarding CP, it can be noted that (61), is the post-FFT data. Let us assume that the overall SER of the system is P_E. We also assume that the SER of the m^{th} subband is P_E^m and that from the n^{th} subcarrier is $P_E^{m,n}$. Considering the N_z zeros, we can now write P_E as

$$P_E = \frac{1}{M}\sum_{m=0}^{M-1} P_E^m = \frac{1}{M(N-N_z)}\sum_{m=0}^{M-1}\sum_{n=0}^{N-N_z-1} P_E^{m,n}. \tag{59}$$

We propose to find a minimum value of N_z, that meets the required system SER i.e. $P_E \le \gamma_{th}$, where γ_{th} is the maximum SER requirement. If we choose a quadrature amplitude modulation (QAM) of M_1 constellations, then $P_E^{m,n}$ can be expressed as in (62), as shown at the bottom of the next page, where $\sigma_{m,n}^2$ is the variance of the noise plus interference from (61) and it is expressed in (63), as shown at the bottom of the next page. An exhaustive search is conducted for N_z starting from 0, 1, 2, ..., $N-1$, that meets $P_E \le \gamma_{th}$ and we pick the lowest one.

B. OPTIMAL CHOICE OF NUMBER OF SUBBANDS WITH TOLERABLE WIDEBAND EFFECT

The wideband is split into multiple smaller bands where a single path faces almost constant gain. This leads to the MB-OFDM waveform proposal. The number of subbands can be made as large as possible to wipe out the effect of the wideband. However, this increases hardware costs and other design-related complexities. We propose a tentative guideline to choose the number of subbands with the consideration of a tolerable wideband effect. To simplify the process of accounting for this effect in the data model, we propose to include it as a multiplicative effect in the OFDM frequency domain subcarriers. Therefore, we can replace $s^m[n]$ as

$$s^m[n] \to \alpha_n^m s^m[n], \tag{64}$$

where α_n^m is the normalized gain due to non-linearity at the n^{th} subcarrier of the m^{th} subband and its default value is one. Now, ignoring the time change effect due to Doppler, α_n^m can be approximated as

$$\alpha_n^m \approx 1 + \Delta\alpha_n^m, \tag{65}$$

where we define $\Delta\alpha_n^m \triangleq \frac{1}{N_p}\sum_{i=1}^{N_p}\Delta\alpha_{n,i}^m$ and each $\Delta\alpha_{n,i}^m$ can be modelled as in (66), as shown at the bottom of the next page. From (66), $f_{m,n}$ and f_m^c are the frequencies at the n^{th} subcarrier and the $(N/2-1)^{th}$ subcarrier of the m^{th} subband, respectively. Statistically, $\Delta\alpha_n^m$ can be modelled as a non-zero mean Gaussian process with decaying mean $(\epsilon_{m,n})$ and variance $(\sigma_{e,m,n}^2)$ using central limit theorem (CLT). The effective noise variance can be calculated as in (67), as shown at the bottom of page 16.

with $f_{m,n} = f_c - \frac{B}{2} + \frac{B(m-1)}{M} + \frac{B(n-1)}{MN}$ and $f_{m,n}^c = f_c - \frac{B}{2} + \frac{B(m-1)}{M} + \frac{B(N/2-1)}{MN}$.

The interference component in the effective noise power depends on the RF frequency. This is expected as the channel path gains and non-linearity are frequency dependent as evident in (66). Therefore, the choice of M should be dependent on the modulating RF frequency. We now propose a simple guideline to choose the value of M, i.e. the number of subbands. For a fixed bandwidth (BW) and RF, a large M is taken as reference, called M_{ref}. For this M_{ref} value, the non-linear wideband effects are negligible. Calculate a theoretical value of any cost function, say BER or capacity that meets the tolerance value with respect to the reference one. For example with BER, we can formulate the problem from (59) and (67) as follows

$$\arg\min_M |P_E(M) - P_E(M_{ref}) - \gamma_{BER}|, \tag{69}$$

where γ_{BER} is the desired tolerance limit and P_E is as defined in (59). A simple line search will solve the optimization problem.

Remarks: Parameters $\epsilon_{m,n}$ and $\sigma^2_{e,m,n}$ are difficult to obtain in practice. Therefore, these parameters need to be synthetically generated using simulations. Another inaccurate method is through the estimated eigenvalues of the effective channel. We can ignore the estimation error if the data points are averaged over multiple estimations.

IX. NUMERICAL RESULTS

In this section, we provide the numerical results and discussion to illustrate the performance of the proposed filter bank-based transmitted waveform model for wideband THz communication system under different system parameter assumptions. We consider a wideband THz system deploying

$$\begin{aligned} Y_d^m(\omega) &= \frac{1}{M}\sum_{k=0}^{M-1} Y\left(e^{j(\omega-2\pi k+m\pi)/M}\right) H_2\left(e^{j(\omega-2\pi k)/M}\right) \\ &= \frac{1}{M}\sum_{k=0}^{M-1}\left[\sum_{p=0}^{M-1} H_p^c\left(e^{j(\omega-2\pi k+m\pi)/M}\right) X^p\left(e^{j(\omega-2\pi k+m\pi-p\pi)/M}\right) H_1\left(e^{j(\omega-2\pi k+m\pi-p\pi)/M}\right)\right] \\ &\quad \times e^{-j\omega M} H_2\left(e^{j(\omega-2\pi k)/M}\right) \\ &= \frac{1}{M\sqrt{N}}\sum_{k=0}^{M-1}\left[\sum_{p=0}^{M-1} H_p^c\left(e^{i(\omega-2\pi k+m\pi)/M}\right)\left[\sum_{l=0}^{N+L_c-1}\left[\sum_{q=0}^{N-1} e^{-j2\pi ql/N} s^m[q]\right] e^{-j(\omega-2\pi k+m\pi-p\pi)l/M}\right]\right. \\ &\quad \left.\times H_1\left(e^{j(\omega-2\pi k+m\pi-p\pi)/M}\right)\right] e^{-j\omega M} H_2\left(e^{j(\omega-2\pi k)/M}\right) + W(\omega), \end{aligned} \tag{60}$$

$$\begin{aligned} Y_d^m(n) \approx \underbrace{\frac{1}{M\sqrt{N}}\left[H_m^c\left(e^{i(2\pi n/N+m\pi)/M}\right)\left[\sum_{l=0}^{N-1}\left[\sum_{q=0}^{N-1} e^{-j2\pi ql/N} s^m[n]\right] e^{-j2\pi nl/NM}\right] H_1\left(e^{j2\pi n/NM}\right)\right] e^{-j2\pi nM/N} H_2\left(e^{j2\pi n/MN}\right)}_{\text{data}} \\ + \frac{1}{M\sqrt{N}}\left[\sum_{p=m-1,p\neq m}^{m+1} H_p^c\left(e^{i(2\pi n/N-2\pi+m\pi)/M}\right)\left[\sum_{l=0}^{N-1}\left[\sum_{q=0}^{N-1} e^{-j2\pi ql/N} s^m[q]\right] e^{-j(2\pi n/N-2\pi+m\pi-p\pi)l/M}\right]\right. \\ \left.\times H_1\left(e^{j(2\pi n/N-2\pi+m\pi-p\pi)/M}\right)\right] e^{-j2\pi nM/N} H_2\left(e^{j(2\pi n/N-2\pi)/M}\right) + W[n], \\ [\text{with } n = 0, 1, \ldots, N-1]. \end{aligned} \tag{61}$$

$$P_E^{m,n} \approx 4\left(1-\frac{1}{\sqrt{M_1}}\right) Q\left(\frac{a}{\sigma_{m,n}}\right)\left[1+Q^2\left(\frac{a}{\sigma_{m,n}}\right)\left(1-\frac{1}{\sqrt{M_1}}\right)\right]. \tag{62}$$

$$\sigma^2_{m,n} = \frac{\frac{(N-N_z)\sigma_s^2}{N}\left[\sum_{p=m-1,m+1} \| H_p^c\left(e^{i(2\pi n/N-2\pi+m\pi)/M}\right) H_1\left(e^{j(2\pi n/N-2\pi+m\pi-p\pi)/M}\right) H_2\left(e^{j(2\pi n/N-2\pi k)/M}\right)\|^2\right] + \sigma_w^2}{\frac{(N-N_z)\sigma_s^2}{N}\| H_m^c\left(e^{i(2\pi n/N+m\pi)/M}\right) H_1\left(e^{j2\pi n/NM}\right) H_2\left(e^{j2\pi n/MN}\right)\|^2}. \tag{63}$$

$$\Delta\alpha_{n,i}^m = \frac{|H_i^F(f_{m,n})||H_i^A(f_{m,n})||H_i^P(f_{m,n})| - |H_i^F(f_m^c)||H_i^A(f_m^c)||H_i^P(f_m^c)|}{|H_i^F(f_m^c)||H_i^A(f_m^c)||H_i^P(f_m^c)|}, \tag{66}$$

$$\sigma^2_{e,m,n} = \frac{I_{m,n}+\sigma_w^2}{\frac{(N-N_z)\sigma_s^2}{N}\| H_m^c\left(e^{i(2\pi n/N+m\pi)/M}\right) H_1\left(e^{j2\pi n/NM}\right) H_2\left(e^{j2\pi n/MN}\right)\|^2}. \tag{67}$$

where the interference term $I_{m,n}$ can be calculated as

a UPA at both the transmitter and receiver. The distance between the neighboring antenna elements in the array is half the wavelength of the signal. The beamforming at the transmitter and the combining at the receiver are implemented in the analog domain using digitally controlled phase shifters. We consider an indoor office scenario, where the transmitter and receiver are kept 5 m apart in three-dimensional (3D) space. We consider 20 reflective/scattering paths of which 10 are plastic, 5 are wood, and 5 are iron in the system. The room temperature is 27^oC. It is assumed that the dominant contributors in air compositions are O_2, and H_2O. The air pressure is assumed to be 101325 pascals, which is the sea level pressure and is considered as reference and actual pressure in simulation. The path gains in each of the subbands are generated using (4) to (7) with HITRAN database [3]. The default RF is assumed to be 200 GHz. In the first scenario, we consider an input signal bandwidth of 20 GHz and split it into 20 number of subbands each with a bandwidth of 1 GHz. In each channel realization, the AoAs and AoDs of the paths are picked from the uniform distribution, i.e. $[-\pi\ \pi]$. Given the stringent energy efficiency demands of THz systems, we have considered the quadrature phase shift keying (QPSK) modulation scheme as the basis for assessing the performance of our proposed system. Other default simulation parameters are shown in Table 1.

TABLE 1. List of pararameters.

Name of parameter	Value
RF carrier frequency (f_c)	200 GHz
Input Bandwidth (Default)	20 GHz
No of Subbands (Default)	20
Modulation (Default)	QPSK
Array type	UPA
FFT Size	4096
No. of Tx Antennas	80×80
No. of Rx Antennas	80×80
No. of Pilot Beams	20
Tx-Rx distance	5 m
No. of scatterers/reflectors/diffractor	20
Antenna position error (From PCB model)	1%
Connector in PCB from PA to the antenna (From Spice model)	Copper
Steering angle circuit inaccuracy	1-5%
Wire length inaccuracy (From PCB design model)	2%
SFO (Obtained from PLL jitter)	0.1% of T_{DAC}/T_{ADC}
Air temperature	25^o C
PCB temperature	25^o C
PA to antenna average length (From PCB design model)	10 mm
Copper temperature resistance coefficient α_t	$0.00385/^oC$
Copper resistivity ρ_{to}	1.722×10^{-11} Ω-mm
Copper inductance per unit length (L_t)	1.1×10^{-9} H/mm
Copper capacitance per unit length (C_t)	0.123×10^{-12} F/mm
PCB board conductivity per unit length (G_t)	0.5×10^{-10} Siemens/mm
Copper thermal expansion coefficient (α_{as})	16.7 ppm
O_2 and H_2O in air	21% and 4%
Air pressure at the sea level	101325 pascals
LMMSE equalizer length	40
Relative permeability μ_r	1 (Copper)

1) BER EVALUATION WITH PROPOSED MB-OFDM WAVEFORM

The BER performance is evaluated with a bandwidth of 20 GHz and RF of 200 GHz. We have used Algorithm-1 for channel estimation. The coefficients from (48) and (49) are obtained experimentally. We first send all pilots on the subcarriers so that the estimation of channel coefficients is done using only (47). To reduce the complexity, we consider only 20 near-by elements for (48). We then conduct curve fitting to find these coefficients. The process is repeated 50 times and then averaged to obtain finer values of the coefficients. A similar exercise is performed for (49).

We plot the BER vs. SNR performance of the proposed waveform in THz system in FIGURE 4 with various QAM constellation along with the proposed squint effect mitigation, precoder and channel estimation. We compare the performance with that of the existing TTD-based squint-mitigated single OFDM system [39]. We observe that even for the 64-QAM case, we obtain an SNR gain of more than 7 dB at BER of 4×10^{-3}. A similar result exists for 256-QAM as well. This shows that the proposed MB-OFDM well mitigates the frequency dependency of the wideband effect along with the proposed squint mitigation and precoder design. The plot in FIGURE 5 is with respect to various zero padding lengths. In this figure, we have used the suboptimal approach of zero-padding, where the number is chosen arbitrarily. It shows that as the number of zero-padding decreases, the BER performance degrades, which is expected. It is also noted that for a lower number of zero-padding, i.e. $N_z = 200$, the BER performance tends to be flat at higher SNR values. This is because as N_z reduces, the sideband interference increases and this component dominates over the AWGN. This sideband interference is given in (61) and its expected value is given in the numerator of (63).

$$I_{m,n} = \frac{(N-N_z)\sigma_s^2(1+\epsilon_{m,n}^2+\sigma_{e,m,n}^2)}{N}\left[\sum_p \|H_p^c\left(e^{j(2\pi n/N-2\pi+m\pi)/M}\right)H_1\left(e^{j(2\pi n/N-2\pi+m\pi-p\pi)/M}\right)H_2\left(e^{j(2\pi n/N-2\pi k)/M}\right)\|^2\right]$$
$$+\left[\frac{(N-N_z)(\epsilon_{m,n}^2+\sigma_{e,m,n}^2)}{N}\|H_m^c\left(e^{j(2\pi n/N+m\pi)/M}\right)H_1\left(e^{j2\pi n/NM}\right)H_2\left(e^{j2\pi n/MN}\right)\|^2\right], \quad (68)$$

with $p = m-1, m+1$.

TABLE 2. Spectral efficiency degradation.

Method	Spectral efficiency degradation
Existing work [23]	14 %
With Proposed N_z	10 %

In FIGURE 6, we plot the performance of the proposed BER-based zero-padding number with respect to a target BER at a fixed SNR of 40 dB. It is noted that the desired target BER depends on the application. We notice that for the target BER of 0.3×10^{-3}, the proposed solution requires only 400 number of zero-padding subcarriers. We have compared the result with [20] and [23], where 530 number of zero-subcarriers are required based on the filter roll-off factor and it does not depend on the BER requirement. Let us define the spectral efficiency degradation as $\frac{N_z + L_c}{N + L_c}$, where L_c, N_z, N are the CP length, number of zero-subcarriers and the total number of subcarriers as defined earlier. Then, from FIGURE 6 with a target BER of 0.3×10^{-3}, the proposed optimized zero-subcarrier scheme ensures almost 10% spectral efficiency degradation, while the work in [23] has almost 14% spectral efficiency degradation as shown in Table 2.

We now plot the BER performance with varying numbers of subbands M in FIGURE 7 with RF of 200 GHz and bandwidth of 20 GHz to capture the wideband effect in a subband. We observe that as we increase M, the BER performance improves. Take the case of $M = 20, 40$. We observe an almost 10 dB SNR improvement at a BER of 3×10^{-4}. The reason behind the improvement is that larger M makes the subband narrower, which removes the wideband and frequency dependency of various THz parameters. However, we also observe that for $M = 30, 40$, the improvement margin is very small. This is expected as the wideband effect is indistinguishable for two narrow subbands. This motivates us to find an optimal M, that meets a certain target BER.

2) CHANNEL ESTIMATION EVALUATION

We now demonstrate the performance of the proposed channel estimation algorithms. As stated earlier, we exploit the intra-band and inter-band correlations for estimation. We first consider pilots to be placed at 50 subcarriers interval at 40 dB. The number of subbands is 20 with a total bandwidth of 20 GHz at the RF of 200 GHz. UPA (80×80) based beamforming is considered with OFDM length of 4096. In FIGURE 8, we demonstrate the channel estimation using Algorithm-1. In this figure, we have plotted the channel eigenvalues (post-FFT) with respect to the golden ones. It is shown that the estimated channel eigenvalues almost match the reference ones. In FIGURE 9, we consider pilots at an interval of 200 subcarriers and notice a degradation in estimation performance. We plot the mean square error (MSE) vs. SNR performance in FIGURE 10 of the proposed algorithms. We compare our result with

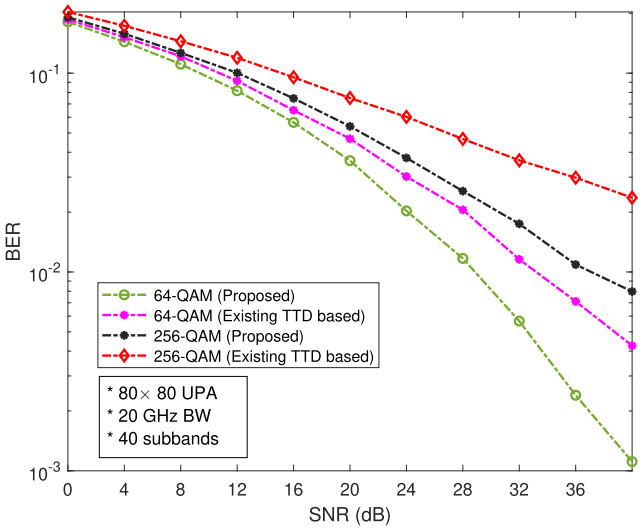

FIGURE 4. Plot of BER of the proposed waveform-based THz system with larger constellation size. We consider a total bandwidth of 20 GHz.

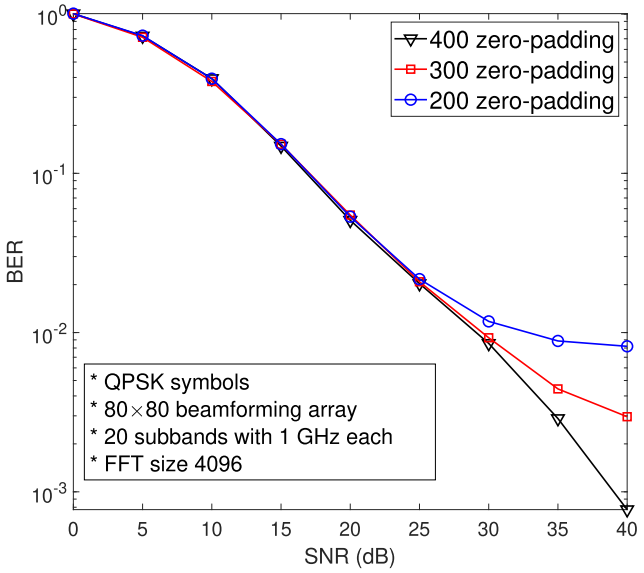

FIGURE 5. BER vs. SNR plots with various zero-padding for avoiding filtering interference. There are 20 subbands with 1 GHz bandwidth each. BW is 20 GHz and RF is 200 GHz.

the existing one from [39]. It can be shown in FIGURE 10 that our proposed channel estimation Algorithms-1,2 are superior in MSE performance to the existing one, as they exploit the inter and intra-subband correlation. Algorithm-2 (DACE) has slightly degraded performance with respect to Algorithm-1, as it is adaptive in nature and has inaccuracy in acquiring parameters. For example, at SNR of 40 dB, existing estimation method obtains MSE of 8×10^{-4}, while Algorithm-1 obtains 2×10^{-4} and Algorithm-2 (DACE) obtains 4×10^{-4}. Next, the MSE performance with Algorithm-1 is plotted in FIGURE 11 with respect to the pilot gaps. We compare the result with the existing work in [39]. In this figure, the MSE performance of Algorithm-1

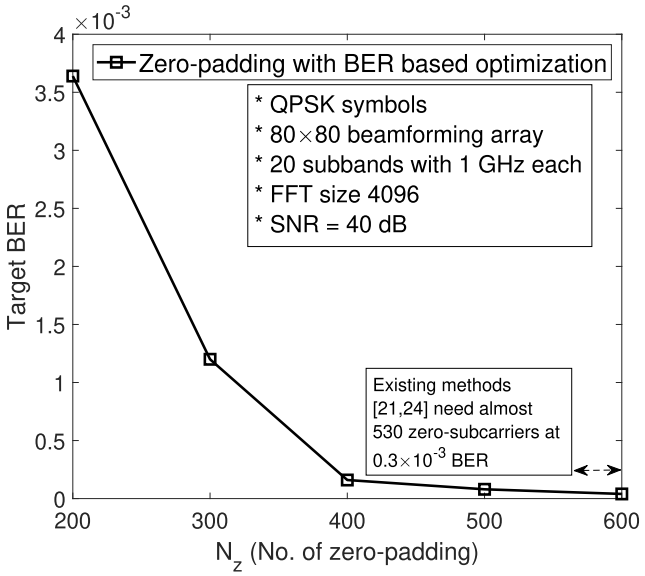

FIGURE 6. Comparison of BER performance with respect to the number of zeros padding effect, where this number is obtained from the proposed BER-based optimization. There are 20-subbands with 1 GHz bandwidth each.

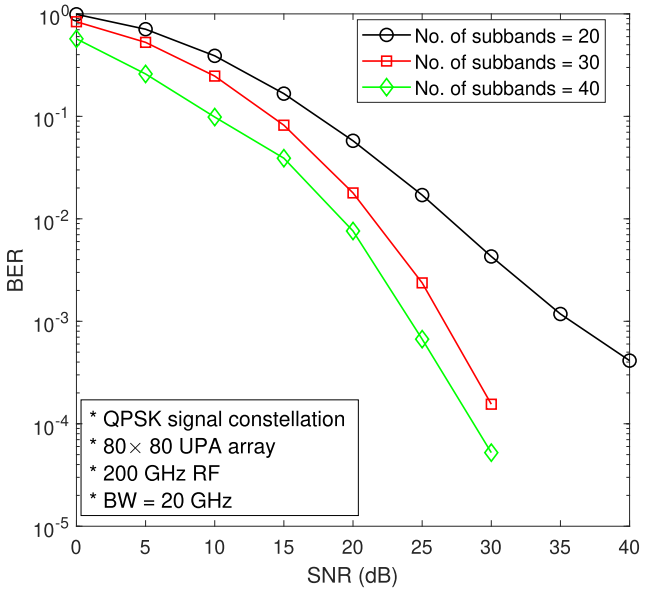

FIGURE 7. Plot of BER of the proposed waveform-based THz system with varying subband numbers. We consider a total bandwidth of 20 GHz.

is also plotted excluding the inter-subband correlation part, which is from (52).It is observed that our proposed algorithm outperforms the existing one. For example, with a pilot gap of 90, our solution obtains an MSE of around 2×10^{-2}, while the existing one attains an MSE of almost 3×10^{-2}. It is also observed that for lesser pilot gaps, MSE performance improves. We have plotted now the BER performance comparisons between the proposed Algorithm-1 and Algorithm-2 in FIGURE 12. We observe that at BER $= 2 \times 10^{-3}$, Algorithm-2 needs 40 dB SNR, while Algorithm-1 needs 36 dB SNR, giving a 4 dB SNR gain. We have also plotted the theoretical probability of error with respect to

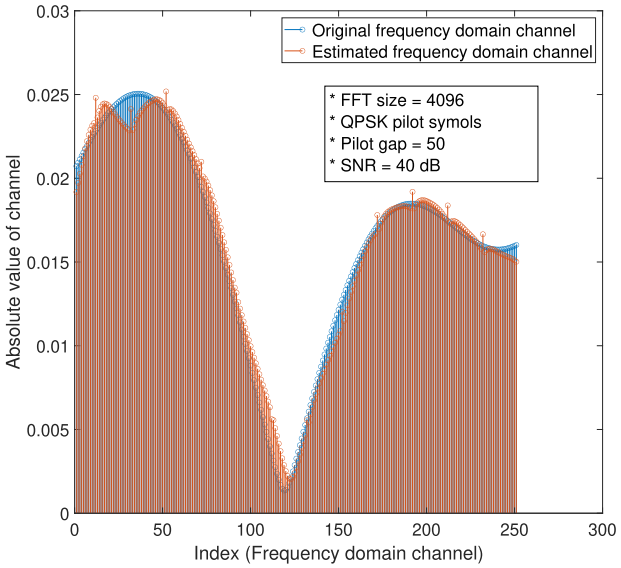

FIGURE 8. Estimated channel taps with pilot gap of 50. BW is kept at 20 GHz with RF of 200 GHz.

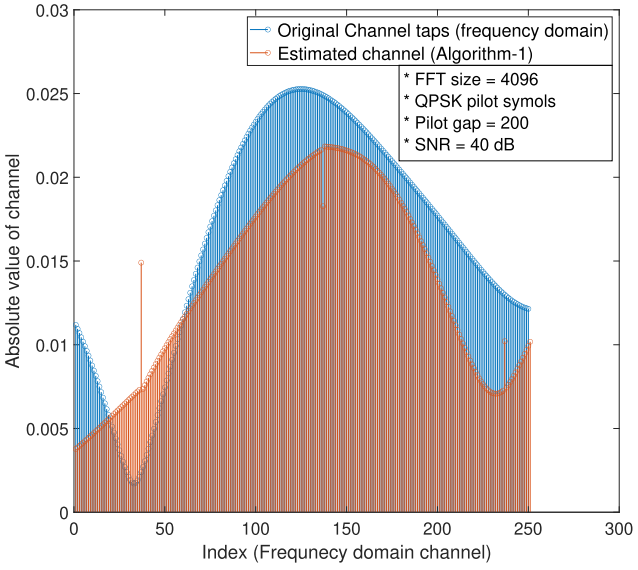

FIGURE 9. Estimated channel taps with pilot gap of 200. BW is kept at 20 GHz with RF of 200 GHz.

Algorithm-1, which is almost matching with the simulated one.

3) OPTIMAL CHOICE OF NUMBER OF SUBBANDS

We now evaluate the optimal choice of subbands for a given bandwidth. This is evaluated with respect to the varying carrier frequency, f_c. In this experiment setup, we have used 20 GHz bandwidth. We have generated the $\Delta\alpha_{n,i}^{m}$ instead of $\epsilon_{m,n}$ and $\sigma_{e,m,n}^{2}$ using (66). This is averaged over 1000 realizations using various random AoA, AoD, and random path lengths within 5 m. We have considered $M_{ref} = 50$ as the reference subband number. We have plotted tentative optimal subband number, M, with carrier frequency in FIGURE 13 for two different tolerance limits 10^{-5}, 10^{-4}. The optimal M is obtained from (69) using integer line search. It is shown that with a lower tolerance limit, M has a higher

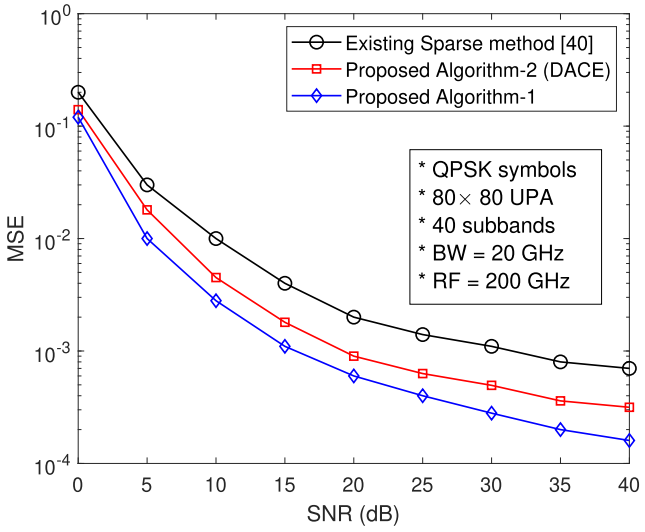

FIGURE 10. Plot of MSE vs. SNR of the estimated channel in the frequency domain with 20 GHz BW and 200 GHz RF.

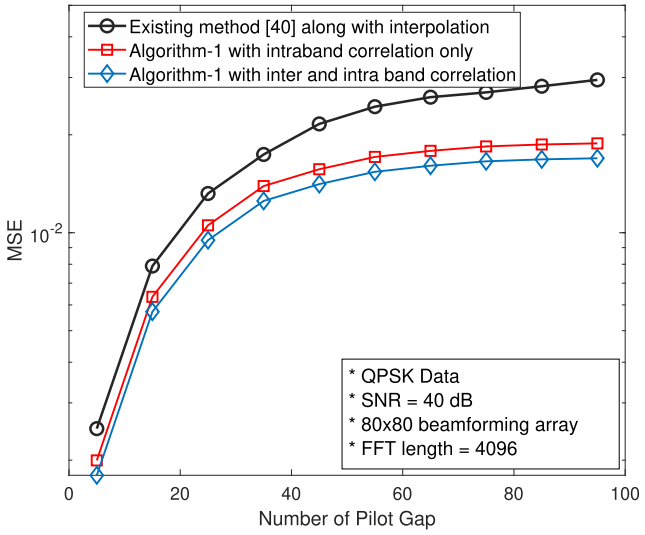

FIGURE 11. Plot of MSE of the estimated channel in the frequency domain with Algorithm-1. We vary the pilot gaps with 20 GHz BW and 200 GHz RF.

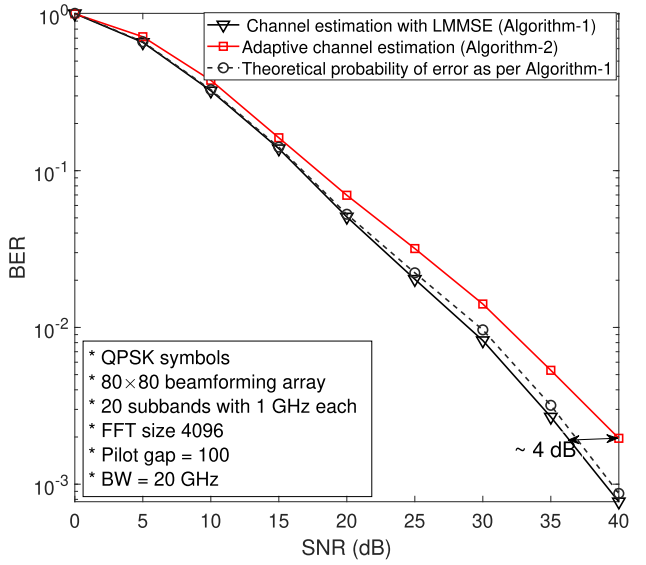

FIGURE 12. Plot of BER of the proposed waveform-based THz system with two different channel estimation algorithms with 20 GHz BW and 200 GHz RF.

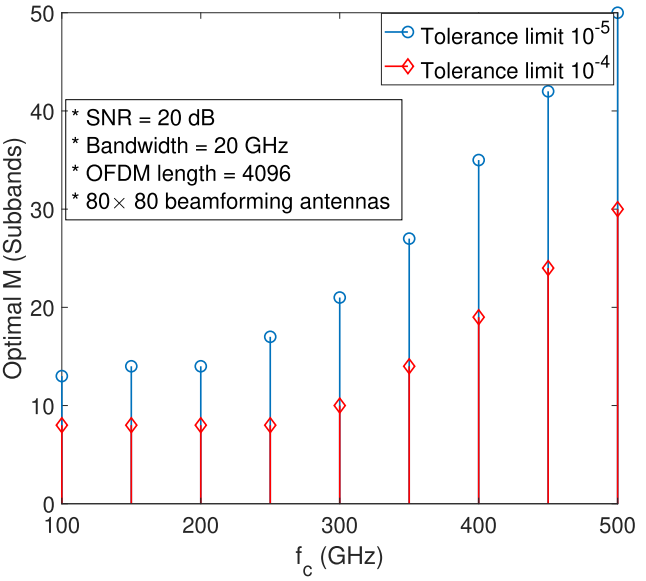

FIGURE 13. Plot for optimal choice of number of subbands (M) vs. carrier frequency (f_c). The SNR is kept at 20 dB, bandwidth is 20 GHz.

value. This is because a lower tolerance limit can be ensured only by a narrower subband bandwidth to remove the effects of the wideband.

4) SQUINT EFFECT MITIGATION

We now demonstrate the proposed impairment-aware LMMSE-based squint effect mitigation. It is to be noted that we obtain the statistics of various impairments from the system-on-chip (SoC) and PCB design computer-aided design (CAD) environments. It can be argued that the actual values may differ slightly in reality. The key difference from the TTD-based solution is that our proposed scheme can exploit all these statistics, as it is done efficiently in the digital domain. In FIGURE 14, we plot the normalized attenuation vs. frequency for various elevation/azimuth angle error variances with the proposed LMMSE digital mitigation scheme. It is shown that the proposed solution almost nullifies the squint effect when observed after the beamforming antennas. However, we observe an almost 0.8 dB more attenuation fluctuation at 1×10^{-2} rad^2 of angle error variance with the TTD-based solution in [39]. This is because the existing TTD solution does not comprehend the PCB details and their statistics information. In FIGURE 15, we plot the normalized attenuation vs. frequency for various BW options with 80 × 80 UPA configuration keeping the filter length to 40. We observe that as we increase the BW, the squint mitigation performance deteriorates. It is observed that there

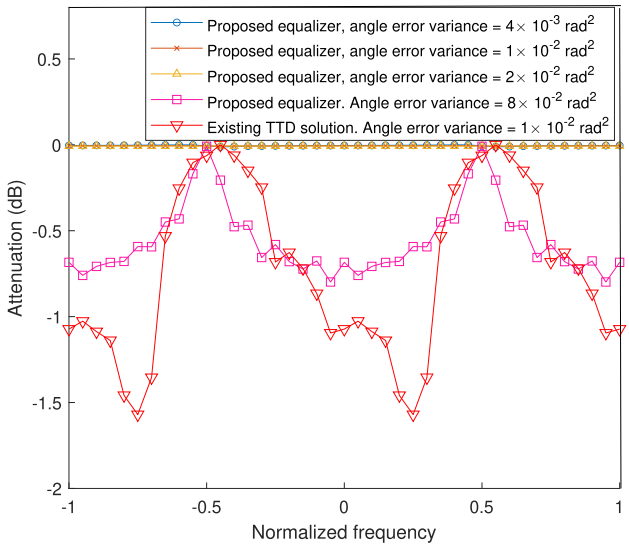

FIGURE 14. Normalized attenuation vs. frequency plot with the proposed LMMSE-based squint mitigation for various elevation/azimuth angle error variance with $f_c = 200$ GHz and BW = 20 GHz with 80 × 80 UPA configuration.

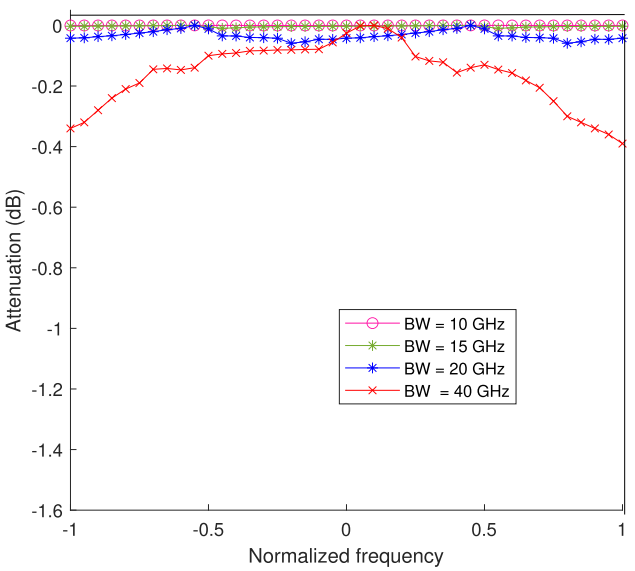

FIGURE 15. Normalized attenuation vs. frequency plot with the proposed LMMSE-based squint mitigation for various BW options with $f_c = 200$ GHz, 80 × 80 UPA configuration and equalizer length of 40.

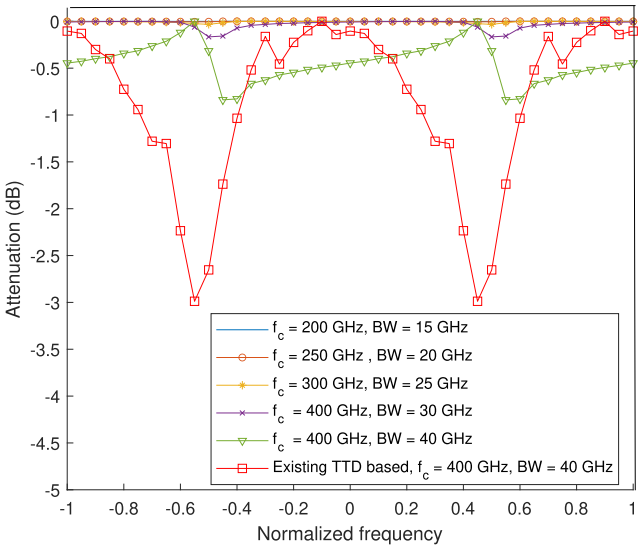

FIGURE 16. Normalized attenuation vs. frequency plot with the proposed LMMSE-based squint mitigation for various BW and f_c options with 80 × 80 UPA configuration and equalizer length of 40.

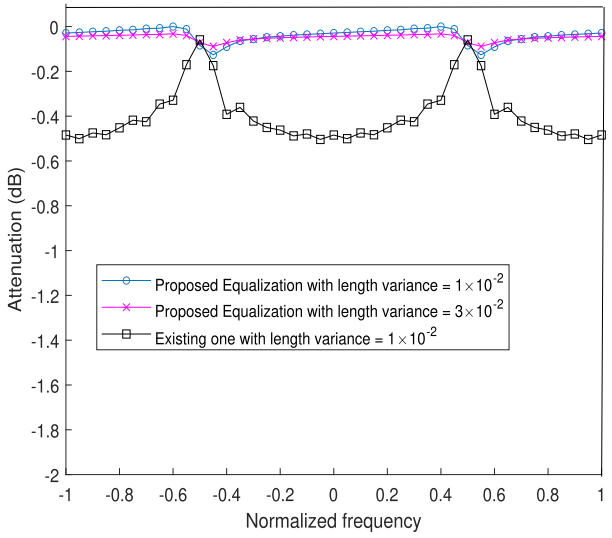

FIGURE 17. Normalized attenuation vs. frequency plot with the proposed LMMSE-based squint mitigation for various PA-to-antenna wire length error variances on PCB board with BW = 20 GHz and $f_c = 200$ GHz with 80 × 80 UPA configuration.

is an attenuation fluctuation exceeding 0.3 dB at a bandwidth of 40 GHz compared to that at 10 GHz. This is because with the large antenna configuration, the equivalent channel due to the squint effect becomes more frequency selective and we need more equalizer length to counter it. This suggests an appropriate equalizer length adjustment. A similar diagram is shown in FIGURE 16 with the variations of BW and f_c. Our proposed solution almost compensates the squint effects compared to the existing TTD-based solution [39], which shows almost 2 dB more attenuation compared to the proposed one at 400 GHz RF with 40 GHz BW.

We now demonstrate the squint mitigation performance with the variation of PA-to-antenna connection wire length error variance present in the PCB board. From FIGURE 17, we show that the squint effect is well mitigated for two example cases with error variance 1×10^{-2}, 3×10^{-2} compared to the existing TTD based solution with variance 1×10^{-2}, which has a fluctuation of almost 0.5 dB.

We now demonstrate the proposed squint mitigation with SFO and temperature variations. In FIGURE 18, we vary the SFO from $(1 - 3)\%$ of the T_{DAC}. It is observed that the proposed LMMSE-based mitigation does a fairly good job, while the existing solution shows a degradation of about

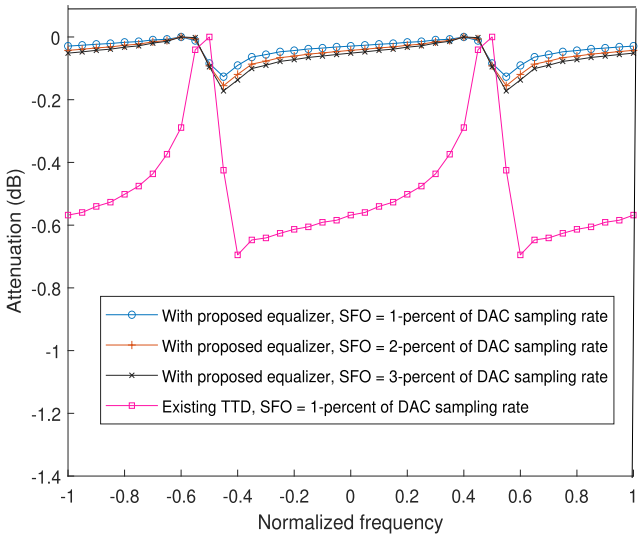

FIGURE 18. Normalized attenuation vs. frequency plot with the proposed LMMSE-based squint mitigation for various SFO values with BW = 20 GHz and f_c = 200 GHz with 80 × 80 UPA configuration.

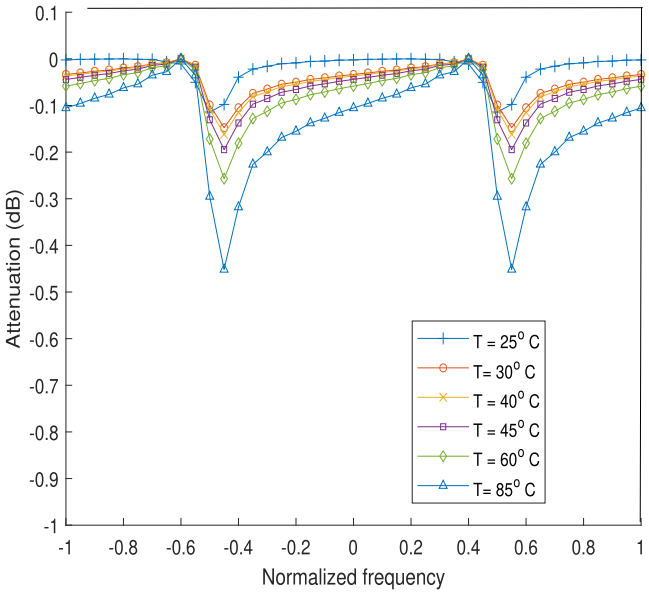

FIGURE 19. Normalized attenuation vs. frequency plot with the proposed LMMSE-based squint mitigation for various temperatures in the board with BW = 20 GHz and f_c = 200 GHz with 80 × 80 UPA configuration.

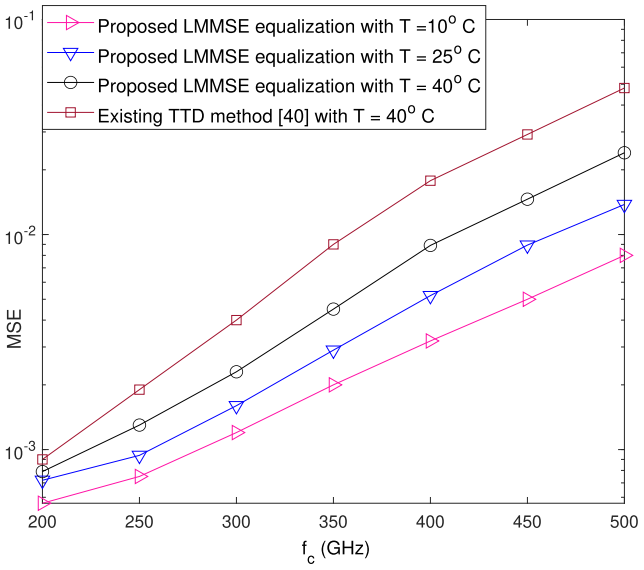

FIGURE 20. MSE vs. f_c plot with the proposed LMMSE-based squint mitigation for different temperatures with BW to f_c ratio fixed at 0.1, 80 × 80 UPA configuration.

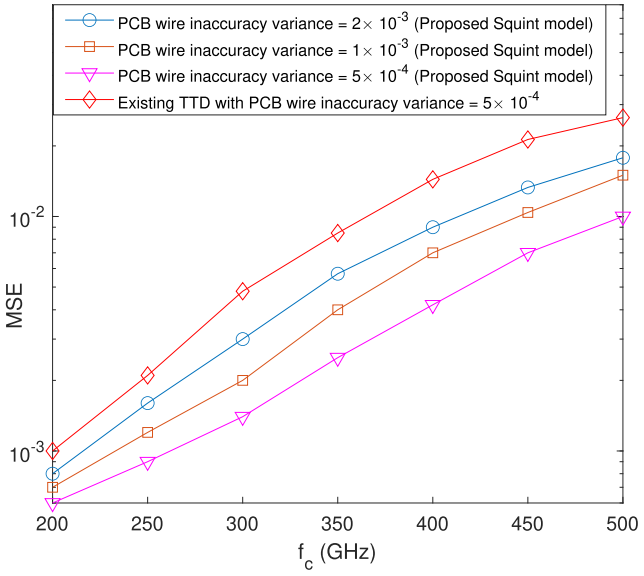

FIGURE 21. MSE vs. f_c plot with the proposed LMMSE-based squint mitigation for different PCB wire inaccuracy variance with BW to f_c ratio fixed at 0.1.

0.8 dB for 1% SFO. This may further degrade with higher SFO. In FIGURE 19, we vary the temperature and observe the squint mitigation. It can be observed that with the higher temperature, the proposed solution shows degradation in performance. At 85^{o}C, we observe almost 0.4 dB more attenuation. This is because as the temperature increases, effective noise component $\epsilon_h[p]$ from (42) also increases and hence the performance degradation.

We now demonstrate the MSE performance vs f_c as per (45) for the proposed squint mitigation. We keep the BW to RF (f_c) ratio fixed at 0.1. In FIGURE 20, we plot the MSE for different temperatures. We observe an MSE improvement of 2.5 × 10^{-2} at a temperature of 40^{o}C, when compared to the TTD-based solution [39] at 400 GHz RF. It is also observed that the MSE performance degrades with higher RF frequency. This occurs because the higher frequency induces more skinning effects in the wire, subsequently degrading the performance. Additionally, higher temperatures lead to increased resistance and a slight lengthening of the wire, both of which contribute to the degradation of performance. FIGURE 21 plots the MSE for various PCB connection wire inaccuracy variances. We see an expected MSE degradation

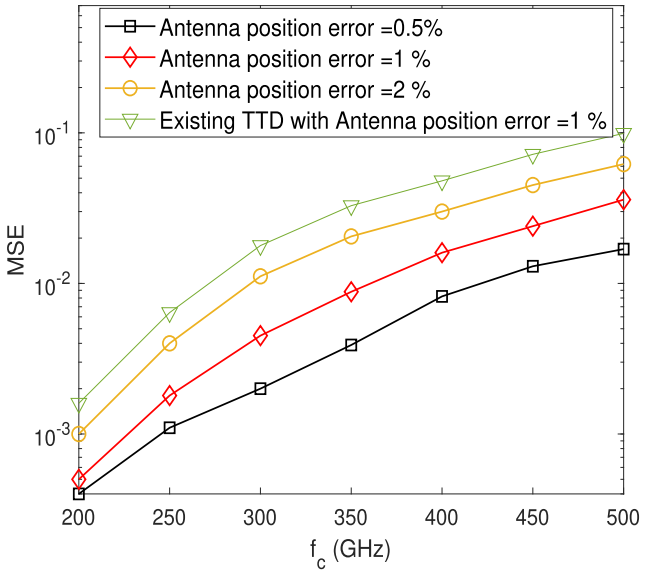

FIGURE 22. MSE vs. f_c plot with the proposed LMMSE-based squint mitigation for different antenna position errors with BW to f_c ratio fixed at 0.1.

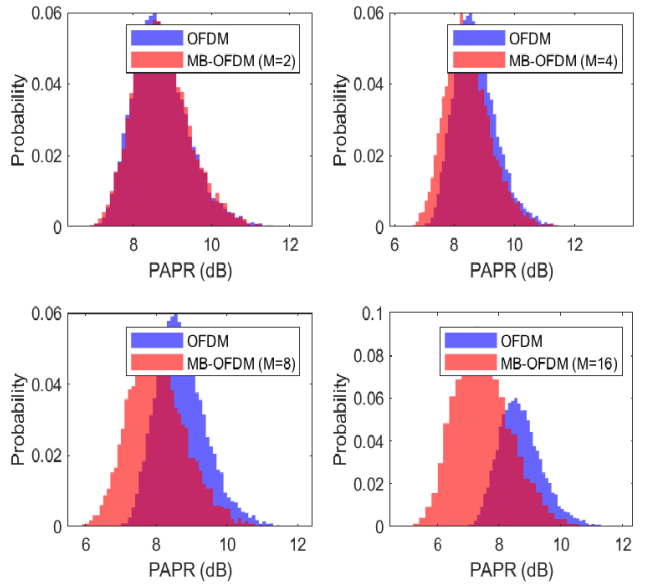

FIGURE 23. Histogram showing PAPR comparison of the proposed THz MB-OFDM baseband waveform with conventional OFDM with BW = 20 GHz and the number of subcarriers= 1024.

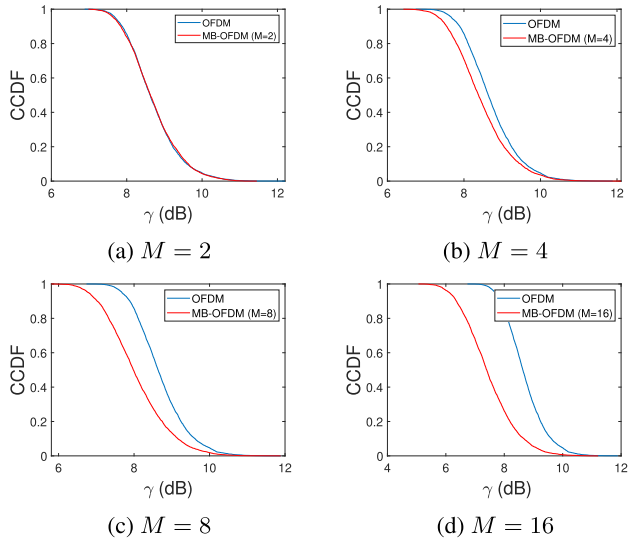

FIGURE 24. PAPR comparison in terms of CCDF for proposed THz MB-OFDM baseband waveform and conventional OFDM with BW = 20 GHz and the number of subcarriers= 1024.

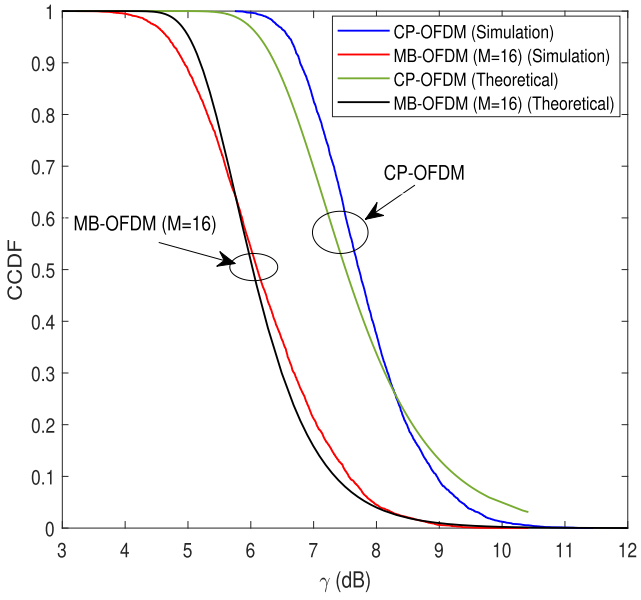

FIGURE 25. PAPR comparison for proposed THz MB-OFDM baseband waveform and conventional OFDM in terms of CCDF with the approximated theoretical expression for M = 16 and total number of subcarriers = 1024.

with higher connection wire inaccuracy variance. It is observed that for a connection wire length error variance of 5×10^{-4}, the proposed scheme shows superior performance compared to the existing TTD-based solution [39] with the same wire length error variance. Finally, FIGURE 22 plots the MSE for various antenna position errors. In this case, the MSE performance degrades with higher RF frequency and higher antenna position errors as expected. However, the proposed scheme exhibits an MSE performance improvement as compared to the existing TTD solution [39]. We observe that the existing scheme obtains an MSE of 4×10^{-2}, while our proposed squint model and mitigation scheme attains 2×10^{-2} MSE at 400 GHz RF with an antenna position error of 1%.

5) PAPR COMPARISON OF THE PROPOSED WAVEFORM WITH CONVENTIONAL OFDM

In this section, we present the simulation results of our proposed MB-OFDM THz waveform in terms of PAPR when compared to conventional OFDM under identical bandwidth conditions. To illustrate the distribution of PAPR of discrete-time baseband OFDM and the proposed MB-OFDM signals, we have plotted histograms averaged over

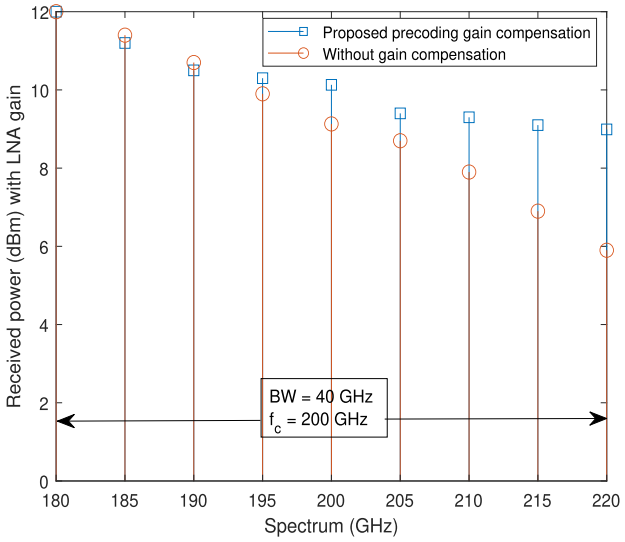

FIGURE 26. Received power gain compensation due to wideband effects in path loss and environmental attenuation for 40 GHz BW. O_2 and H_2O are 21% and 3%.

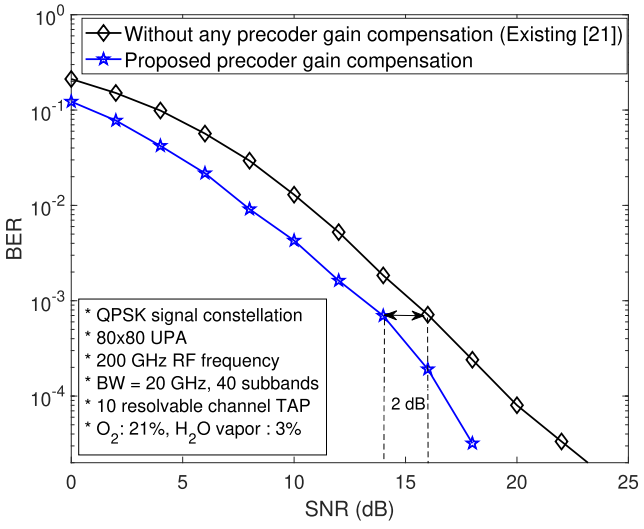

FIGURE 27. BER plot with the proposed precoder gain compensation for a bandwidth of 20 GHz at $f_c = 200$ GHz. O_2 and H_2O are 21% and 3%.

several realizations. Then the PAPR performance is compared for both schemes in terms of the CCDF of PAPR. We assume a bandwidth of 20 GHz and the total number of subcarriers as 1024 with the QPSK modulation scheme. It means that $M \times N = 1024$, which ensures that it is a fair comparison between OFDM ($M = 1$) and the MB-OFDM ($M > 1$) keeping the overall number of subcarriers constant. The simulation results in terms of histograms in FIGURE 23 and the corresponding CCDFs in FIGURE 24 show a reduction in PAPR for the proposed MB-OFDM over the conventional OFDM. From FIGURE 23, while single OFDM shows a mean PAPR value of 8.92 dB, the proposed MB-OFDM has mean PAPR values reduced to 8.72, 8.46, 8.03, and 7.48 for $M = 2$, $M = 4$, $M = 8$, and $M = 16$, respectively. If we keep $M \times N$ constant and increase the subband number M, the PAPR decreases as per (18) and this is evident in FIGURE 24. This shows that the proposed MB-OFDM scheme accomplishes a notable reduction in the PAPR through the THz-specific baseband design that divides the wideband into smaller subbands. It is also evident from (18) and [16], [44], and [45] that the front-end filter after upsampling in each subband can increase the PAPR. However, this effect can be offset by the lower number of subcarriers in each subband causing a reduction in peak power [52] and thereby decreasing the likelihood of having peaks in all the subbands at the same time resulting in an overall reduction in PAPR as compared to a single wideband OFDM signal. In FIGURE 25, the approximated theoretical result from (18) is compared with the conventional OFDM and the simulated results for $M = 16$. This is in agreement with our simulation results showing a reduction in PAPR with the increase in the number of subbands, provided $M \times N$ is kept constant.

6) PROPOSED ENVIRONMENT AWARE PRECODING GAIN

We now demonstrate the performance of the proposed precoding gain adjustment for almost equal gains over the large bandwidth. In this simulation, we have considered $P = 10$ resolvable channel tap gains at the baseband after the ADC sampling. Overall 40 GHz band of occupancy is assumed around 200 GHz RF. We have also considered a sea level height for the system, which has a typical air pressure of 101325 pascals. However, the exact air pressure can be obtained from the sensor. The air composition assumes that the O_2 is 21% and H_2O is 3%. As discussed in [3], the key attenuation effect is from H_2O in $200 - 1000$ GHz. The exact air composition will be from the sensors. The attenuation factor $k(f_m)$ at any frequency f_m is calculated as per the standard work in [3]. The line-of-sight (LoS) distance is measured as per work in [53]. The rest of the distances are interpolated using the T_{ADC} and path index from $2 \ldots 10$. We also assume that the inaccuracy in LoS distance measurement is $\pm 5\%$ with uniform distribution.

From FIGURE 26, we observe that without gain compensation as in [39], the loss is almost 5.5 dB at around 220 GHz. But with the proposed gain compensation, almost 2.8 dB loss is recovered at 220 GHz compared to 180 GHz. We could not gain more due to the fact that the wideband scattering and reflection effects are not compensated in this proposal. This is because we do not know the exact material that scatters/reflects invisible waves. We also plot the BER improvement due to gain compensation in FIGURE 27. It can be observed that there is an SNR gain of almost 2 dB at around the BER of 10^{-4} compared to the existing MB-OFDM based result [20] simulated with THz channel model and squint mitigation. We also give the baseband implementation result of the proposed scheme on the Xilinx FPGA-ZCU111 platform in Table 3 with 20 subbands having 4096-IFFT each. The result includes the MB-OFDM structure, related control circuits, memory, and processor interface. We observe

TABLE 3. Implementation on Xilinx FPGA-ZCU111.

System	Flip-flops	DSP slice	LUT
MB-OFDM (20 subbands)	50763	180	60279
Single OFDM	4276	15	4985

that there is a significant increase in hardware logic for the MB-OFDM baseband implementation. However, the high gate count is due to the parallel implementation of MB-OFDM chains. We could have implemented only a single chain and recursively used as many subbands as required. However, such serial processing may increase processing time.

X. CONCLUSION

In this work, we have presented a wideband THz system with a novel digital baseband waveform design tailored to the unique frequency-dependent channel characteristics specific to THz. We have proposed a system design with a THz-specific MB-OFDM waveform design using a filter bank-based channel model for ultra-wideband THz communication to address the frequency-dependent challenges associated with the wideband THz channel. We have also proposed a channel estimation scheme incorporating the inter-subband and intra-subband correlation to improve the performance. Furthermore, we have introduced a novel squint mitigation scheme in the digital domain, accounting for various impairments from PCB design to circuit imperfections and SFO. This approach eliminates the necessity for expensive and power-intensive TTDs in the RF domain, thereby reducing both power consumption and hardware complexity. We have also proposed an environment-aware precoder design along with the optimal number of zero-subcarriers and subbands for a target BER parameter. Our simulation results also show a reduction in PAPR for the proposed waveform design as compared to conventional OFDM under identical bandwidth conditions. The future direction of the work should be extended to the MIMO systems.

REFERENCES

[1] N. Khalid and O. B. Akan, "Experimental throughput analysis of low-THz MIMO communication channel in 5G wireless networks," *IEEE Wireless Commun. Lett.*, vol. 5, no. 6, pp. 616–619, Dec. 2016.

[2] I. F. Akyildiz, J. M. Jornet, and C. Han, "Terahertz band: Next frontier for wireless communications," *Phys. Commun.*, vol. 12, pp. 16–32, Sep. 2014.

[3] J. M. Jornet and I. F. Akyildiz, "Channel modeling and capacity analysis for electromagnetic wireless nanonetworks in the terahertz band," *IEEE Trans. Wireless Commun.*, vol. 10, no. 10, pp. 3211–3221, Oct. 2011.

[4] C. Han, A. O. Bicen, and I. F. Akyildiz, "Multi-ray channel modeling and wideband characterization for wireless communications in the terahertz band," *IEEE Trans. Wireless Commun.*, vol. 14, no. 5, pp. 2402–2412, May 2015.

[5] R. Piesiewicz, C. Jansen, D. Mittleman, T. Kleine-Ostmann, M. Koch, and T. Kurner, "Scattering analysis for the modeling of THz communication systems," *IEEE Trans. Antennas Propag.*, vol. 55, no. 11, pp. 3002–3009, Nov. 2007.

[6] F. Sheikh, Y. Zantah, I. B. Mabrouk, M. Alissa, J. Barowski, I. Rolfes, and T. Kaiser, "Scattering and roughness analysis of indoor materials at frequencies from 750 GHz to 1.1 THz," *IEEE Trans. Antennas Propag.*, vol. 69, no. 11, pp. 7820–7829, Nov. 2021.

[7] C. L. Vernold and J. E. Harvey, "Modified Beckmann–Kirchoff scattering theory for nonparaxial angles," *Proc. SPIE*, vol. 3426, pp. 51–56, Apr. 1998.

[8] C.-L. Cheng and A. Zajic, "Characterization of propagation phenomena relevant for 300 GHz wireless data center links," *IEEE Trans. Antennas Propag.*, vol. 68, no. 2, pp. 1074–1087, Feb. 2020.

[9] K. Guan, B. Peng, D. He, J. M. Eckhardt, S. Rey, B. Ai, Z. Zhong, and T. Kürner, "Channel characterization for intra-wagon communication at 60 and 300 GHz bands," *IEEE Trans. Veh. Technol.*, vol. 68, no. 6, pp. 5193–5207, Jun. 2019.

[10] J. M. Eckhardt, V. Petrov, D. Moltchanov, Y. Koucheryavy, and T. Kurner, "Channel measurements and modeling for low-terahertz band vehicular communications," *IEEE J. Sel. Areas Commun.*, vol. 39, no. 6, pp. 1590–1603, Jun. 2021.

[11] M. Kokkonen, H. Juttula, A. Mäkynen, S. Myllymäki, and H. Jantunen, "The effect of drop shape, sensing volume and raindrop size statistics to the scattered field on 300 GHz," *IEEE Access*, vol. 9, pp. 101381–101389, 2021.

[12] M. Mandehgar and D. R. Grischkowsky, "Understanding dispersion compensation of the THz communication channels in the atmosphere," *IEEE Photon. Technol. Lett.*, vol. 27, no. 22, pp. 2387–2390, Nov. 12, 2015.

[13] S. Priebe and T. Kurner, "Stochastic modeling of THz indoor radio channels," *IEEE Trans. Wireless Commun.*, vol. 12, no. 9, pp. 4445–4455, Sep. 2013.

[14] K. Tsujimura, K. Umebayashi, J. Kokkoniemi, J. Lehtomäki, and Y. Suzuki, "A causal channel model for the terahertz band," *IEEE Trans. THz Sci. Technol.*, vol. 8, no. 1, pp. 52–62, Jan. 2018.

[15] C. Han, A. O. Bicen, and I. F. Akyildiz, "Multi-wideband waveform design for distance-adaptive wireless communications in the terahertz band," *IEEE Trans. Signal Process.*, vol. 64, no. 4, pp. 910–922, Feb. 2016.

[16] S. Tarboush, H. Sarieddeen, M.-S. Alouini, and T. Y. Al-Naffouri, "Single- versus multicarrier terahertz-band communications: A comparative study," *IEEE Open J. Commun. Soc.*, vol. 3, pp. 1466–1486, 2022.

[17] P. P. Vaidyanathan, *Multirate Systems and Filter Banks*. Upper Saddle River, NJ, USA: Prentice-Hall, 1993.

[18] T. Mao, J. Chen, Q. Wang, C. Han, Z. Wang, and G. K. Karagiannidis, "Waveform design for joint sensing and communications in millimeter-wave and low terahertz bands," *IEEE Trans. Commun.*, vol. 70, no. 10, pp. 7023–7039, Oct. 2022.

[19] Z. Hossain and J. M. Jornet, "Hierarchical bandwidth modulation for ultra-broadband terahertz communications," in *Proc. IEEE Int. Conf. Commun. (ICC)*, May 2019, pp. 1–7.

[20] R. Zakaria and D. Le Ruyet, "A novel filter-bank multicarrier scheme to mitigate the intrinsic interference: Application to MIMO systems," *IEEE Trans. Wireless Commun.*, vol. 11, no. 3, pp. 1112–1123, Mar. 2012.

[21] R. Gerzaguet, D. Demmer, J.-B. Doré, and D. Ktiénas, "Block-filtered OFDM: A new promising waveform for multi-service scenarios," in *Proc. IEEE Int. Conf. Commun. (ICC)*, Oct. 2017, pp. 1–6.

[22] R. Zakaria and D. Le Ruyet, "Theoretical analysis of the power spectral density for FFT-FBMC signals," *IEEE Commun. Lett.*, vol. 20, no. 9, pp. 1748–1751, Sep. 2016.

[23] D. Demmer, R. Zakaria, R. Gerzaguet, J.-B. Doré, and D. Le Ruyet, "Study of OFDM precoded filter-bank waveforms," *IEEE Trans. Wireless Commun.*, vol. 18, no. 6, pp. 2889–2902, Jun. 2019.

[24] B. Peng, S. Wesemann, K. Guan, W. Templ, and T. Kürner, "Precoding and detection for broadband single carrier terahertz massive MIMO systems using LSQR algorithm," *IEEE Trans. Wireless Commun.*, vol. 18, no. 2, pp. 1026–1040, Feb. 2019.

[25] L. Yan, "A dynamic-subarray architecture with low-resolution phase shifters for hybrid precoding in the terahertz band," in *Proc. IEEE Int. Conf. Commun. Workshops*, Jun. 2020, pp. 1–5.

[26] S. A. Busari, S. Mumtaz, and J. Rodriguez, "Hybrid precoding techniques for THz massive MIMO in hotspot network deployment," in *Proc. IEEE 91st Veh. Technol. Conf.*, Jul. 2020, pp. 1–6.

[27] Q. Wan, J. Fang, Z. Chen, and H. Li, "Hybrid precoding and combining for millimeter wave/sub-THz MIMO-OFDM systems with beam squint effects," *IEEE Trans. Veh. Technol.*, vol. 70, no. 8, pp. 8314–8319, Aug. 2021.

[28] V. Petrov, J. Kokkoniemi, D. Moltchanov, J. Lehtomäki, M. Juntti, and Y. Koucheryavy, "The impact of interference from the side lanes on mmWave/THz band V2V communication systems with directional antennas," *IEEE Trans. Veh. Technol.*, vol. 67, no. 6, pp. 5028–5041, Jun. 2018.
[29] S. Jia, X. Yu, H. Hu, J. Yu, T. Morioka, P. U. Jepsen, and L. K. Oxenløwe, "120 Gb/s multi-channel THz wireless transmission and THz receiver performance analysis," *IEEE Photon. Technol. Lett.*, vol. 29, no. 3, pp. 310–313, Feb. 1, 2017, doi: 10.1109/LPT.2016.2647280.
[30] Z. Chen, X. Ma, B. Zhang, Y. Zhang, Z. Niu, N. Kuang, W. Chen, L. Li, and S. Li, "A survey on terahertz communications," *China Commun.*, vol. 16, no. 2, pp. 1–35, Feb. 2019.
[31] B. Peng and T. Kürner, "Three-dimensional angle of arrival estimation in dynamic indoor terahertz channels using a forward–backward algorithm," *IEEE Trans. Veh. Technol.*, vol. 66, no. 5, pp. 3798–3811, Nov. 2017.
[32] A. Brighente, M. Cerutti, M. Nicoli, S. Tomasin, and U. Spagnolini, "Estimation of wideband dynamic mmWave and THz channels for 5G systems and beyond," *IEEE J. Sel. Areas Commun.*, vol. 38, no. 9, pp. 2026–2040, Sep. 2020.
[33] M. Mizmizi, D. Tagliaferri, D. Badini, C. Mazzucco, and U. Spagnolini, "Channel estimation for 6G V2X hybrid systems using multi-vehicular learning," *IEEE Access*, vol. 9, pp. 95775–95790, 2021.
[34] S. Nie and I. F. Akyildiz, "Deep kernel learning-based channel estimation in ultra-massive MIMO communications at 0.06–10 THz," in *Proc. IEEE Globecom Workshops (GC Wkshps)*, Dec. 2019, pp. 1–6.
[35] B. Ning, Z. Chen, W. Chen, and Y. Du, "Channel estimation and transmission for intelligent reflecting surface assisted THz communications," in *Proc. IEEE Int. Conf. Commun. (ICC)*, Jun. 2020, pp. 1–7.
[36] X. Ma, Z. Chen, Y. Chi, W. Chen, L. Du, and Z. Li, "Channel estimation for intelligent reflecting surface enabled terahertz MIMO systems," in *Proc. IEEE Int. Conf. Commun. Workshops*, Jun. 2020, pp. 1–6.
[37] X. Ma, Z. Chen, W. Chen, Z. Li, Y. Chi, C. Han, and S. Li, "Joint channel estimation and data rate maximization for intelligent reflecting surface assisted terahertz MIMO communication systems," *IEEE Access*, vol. 8, pp. 99565–99581, 2020.
[38] A. M. Elbir, W. Shi, A. K. Papazafeiropoulos, P. Kourtessis, and S. Chatzinotas, "Terahertz-band channel and beam split estimation via array perturbation model," *IEEE Open J. Commun. Soc.*, vol. 4, pp. 892–907, 2023.
[39] K. Dovelos, M. Matthaiou, H. Q. Ngo, and B. Bellalta, "Channel estimation and hybrid combining for wideband terahertz massive MIMO systems," *IEEE J. Sel. Areas Commun.*, vol. 39, no. 6, pp. 1604–1620, Jun. 2021.
[40] H. Sun, S. Zhang, J. Ma, and O. A. Dobre, "Time-delay unit based beam squint mitigation for RIS-aided communications," *IEEE Commun. Lett.*, vol. 26, no. 9, pp. 2220–2224, Sep. 2022.
[41] J. Wu, S. Kim, and B. Shim, "Parametric sparse channel estimation for RIS-assisted terahertz systems," *IEEE Trans. Commun.*, vol. 71, no. 9, pp. 5503–5518, Jun. 2023.
[42] L. Yan, C. Han, and J. Yuan, "Energy-efficient dynamic-subarray with fixed true-time-delay design for terahertz wideband hybrid beamforming," *IEEE J. Sel. Areas Commun.*, vol. 40, no. 10, pp. 2840–2854, Oct. 2022.
[43] D. Tse and P. Viswanath, *Fundamentals of Wireless Communication*. Cambridge, U.K.: Cambridge Univ. Press, 2005.
[44] A. Skrzypczak, P. Siohan, and J.-P. Javaudin, "Analysis of the peak-to-average power ratio of the oversampled OFDM," in *Proc. IEEE Int. Conf. Acoust. Speech Signal Process.*, vol. 4, Feb. 2006, pp. 1–4.
[45] M. Chafii, J. Palicot, and R. Gribonval, "Closed-form approximations of the papr distribution for multi-carrier modulation systems," in *Proc. 22nd Eur. Signal Process. Conf. (EUSIPCO)*, 2014, pp. 1920–1924.
[46] C. Y. Ho and R. E. Taylor, *Thermal Expansion of Solids: V. I-4* (CINDAS Data Series on Material Properties). Almere, The Netherlands: ASM Int., 1998.
[47] J. H. Dellinger, *The Temperature Coefficient of Resistance of Copper*. London, U.K.: Forgotten Books, 2018.
[48] X. Li and H. Qiu, "Study on channel estimation for UWB MB-OFDM," in *Proc. Int. Conf. Commun. Technol.*, Nov. 2006, pp. 1–4.
[49] Z. Li, W. Xiuzhen, and H. Yanyan, "An effective channel estimation algorithm for MB-OFDM-UWB system," in *Proc. 10th Int. Conf. Commun. Softw. Netw. (ICCSN)*, Jul. 2018, pp. 26–29.
[50] S. M. Riazul Islam and K. S. Kwak, "Energy-efficient channel estimation for MB-OFDM UWB system in presence of interferences," in *Proc. Int. Conf. Inf. Commun. Technol. Converg. (ICTC)*, Nov. 2010, pp. 149–154.
[51] Y. Wan, A. Liu, Q. Hu, M. Zhang, and Y. Cai, "Multiband delay estimation for localization using a two-stage global estimation scheme," *IEEE Trans. Wireless Commun.*, vol. 22, no. 12, pp. 9263–9277, Dec. 2023.
[52] H. Ochiai and H. Imai, "On the distribution of the peak-to-average power ratio in OFDM signals," *IEEE Trans. Commun.*, vol. 49, no. 2, pp. 282–289, Feb. 2001.
[53] B. Alavi and K. Pahlavan, "Modeling of the TOA-based distance measurement error using UWB indoor radio measurements," *IEEE Commun. Lett.*, vol. 10, no. 4, pp. 275–277, Apr. 2006.

T.D DHEERAJLAL (Graduate Student Member, IEEE) received the B.Tech. degree in electronics and communication engineering from MG University, India, and the M.Tech. degree from Cochin University, India. He is currently pursuing the Ph.D. degree with the G. S. Sanyal School of Telecommunications, Indian Institute of Technology Kharagpur, Kharagpur, India. His current research interests include wireless communication systems design, massive MIMO, OFDM, mmWave, and THz communications system design.

ANKAM MADHUSREE (Student Member, IEEE) received the B.E. degree in electronics and telecommunication from Indian University and the M.Tech. degree from the Indian Institute of Technology Kharagpur, India. She is currently with Qualcomm Pvt. Ltd., India. Her current research interests include 5G wireless communication systems design, massive MIMO, OFDM, mmWave, and THz communications system design.

AMIT KUMAR DUTTA (Member, IEEE) received the B.E. degree in electronics and telecommunication engineering from IIEST, Shibpur, India, and the Ph.D. degree from the Indian Institute of Science, Bengaluru, India. He is currently an Assistant Professor with the G. S. Sanyal School of Telecommunications, Indian Institute of Technology Kharagpur, Kharagpur, India. Prior to joining academics, he was with Texas Instrument (TI) Pvt. Ltd., Broadcom Ltd., Cypress Semiconductor, and NxP Ltd., for a total of almost 14 years. He has elaborate work experience in the field of signal processing, communication, and VLSI design in corporate, which included wireless system design, validation, and characterization. His current research interests include wireless communication systems design, massive MIMO, OFDM, mmWave, THz communications system design, and quantum signal processing.